

# 1 Deforestation as an anthropogenic driver of

## 2 mercury pollution

3 Aryeh Feinberg<sup>a\*</sup>, Martin Jiskra<sup>b\*</sup>, Pasquale Borrelli<sup>c</sup>, Jagannath Biswakarma<sup>b,d</sup>, and

4 Noelle E. Selin<sup>a,e</sup>

5 <sup>a</sup> Institute for Data, Systems, and Society, Massachusetts Institute of Technology,  
6 Cambridge, MA 02139, USA

7 <sup>b</sup> Environmental Geosciences, University of Basel, Basel 4056, Switzerland

8 <sup>c</sup> Department of Science, Roma Tre University, Rome 00146, Italy

9 <sup>d</sup> Department of Water Resources and Drinking Water, Eawag, Dübendorf 8600,  
10 Switzerland

11 <sup>e</sup> Department of Earth, Atmospheric, and Planetary Sciences, Massachusetts Institute of  
12 Technology, Cambridge, MA 02139, USA

13 \*Correspondence to: arifeinberg@gmail.com (A.F.); martin.jiskra@gmail.com (M.J.)

14

15 KEYWORDS. Mercury (Hg), land use change, emissions, Minamata Convention,  
16 Amazon rainforest, reforestation, chemical-transport modeling.

17

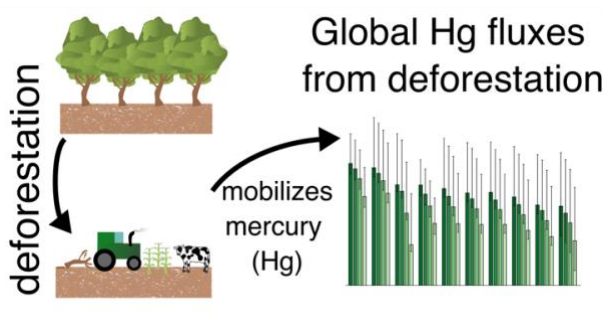
18 **Abstract**

19 Deforestation reduces the capacity of the terrestrial biosphere to take up the toxic  
20 pollutant mercury (Hg) and enhances the release of secondary Hg from soils. The  
21 consequences of deforestation for Hg cycling are not currently considered by  
22 anthropogenic emissions inventories or specifically addressed under the global Minamata  
23 Convention on Mercury. Using global Hg modeling constrained by field observations, we  
24 estimate that net Hg fluxes to the atmosphere due to deforestation are  $217 \text{ Mg yr}^{-1}$  (95%  
25 confidence interval, CI:  $134\text{--}1650 \text{ Mg yr}^{-1}$ ) for 2015, approximately 10% of global  
26 primary anthropogenic emissions. If deforestation of the Amazon rainforest continues at  
27 business-as-usual rates, net Hg emissions from the region will increase by  $153 \text{ Mg yr}^{-1}$  by  
28 2050 (CI:  $97\text{--}418 \text{ Mg yr}^{-1}$ ), enhancing the transport and subsequent deposition of Hg to  
29 aquatic ecosystems. Substantial Hg emissions reductions are found for two potential  
30 cases of land use policies: conservation of the Amazon rainforest ( $92 \text{ Mg yr}^{-1}$ , CI: 59 to  
31  $234 \text{ Mg yr}^{-1}$ ) and global reforestation ( $98 \text{ Mg yr}^{-1}$ , CI: 64 to  $449 \text{ Mg yr}^{-1}$ ). We conclude  
32 that deforestation-related emissions should be incorporated as an anthropogenic source in  
33 Hg inventories, and that land use policy could be leveraged to address global Hg  
34 pollution.

35 **Synopsis**

36 This study quantifies the impact of deforestation on the global Hg cycle, finding that  
37 deforestation increases Hg fluxes to air and water. Conservation and reforestation are  
38 important policy tools to mitigate these fluxes.

39 **TOC Graphic**



41 **Main Text**

42 **Introduction**

43 Humans are exposed to the organic form of mercury (Hg), methylmercury (MeHg),  
44 mainly through seafood consumption<sup>1</sup>. Methylmercury is a potent neurotoxin, impairing  
45 the neurodevelopment of fetuses and children and costing the global economy \$20–117  
46 billion annually according to some estimates<sup>2,3</sup>. Mercury is emitted to the atmosphere by:  
47 a) primary anthropogenic sources, including artisanal and small-scale gold mining  
48 (ASGM), fossil fuel combustion, and metal smelting; b) re-emissions of historical  
49 anthropogenic (“legacy”) Hg from ocean and land; and c) geogenic sources<sup>4</sup>. Mercury  
50 spreads globally in the atmosphere due to its overall elemental lifetime against deposition  
51 of 4–6 months<sup>5</sup>. A global treaty, the Minamata Convention on Mercury, aims to protect  
52 human health and the environment from anthropogenic emissions and releases of Hg. The  
53 Convention targets primary anthropogenic emissions sources by phasing out Hg use and  
54 adopting best available technologies for pollution control<sup>6</sup>. Primary anthropogenic  
55 emissions account for only 30% of present-day total emissions, with legacy re-emissions  
56 from land and ocean accounting for 60%<sup>7</sup>. The future of Hg pollution will depend not  
57 only on reducing direct emissions through the Minamata Convention, but also on indirect  
58 anthropogenic influences on legacy Hg emissions and fate.

59 Terrestrial ecosystems, and especially forests, are important sinks of Hg from the  
60 atmosphere, taking up an estimated 2200–3600 Mg Hg per year<sup>8</sup>, more than a third of  
61 total (anthropogenic, legacy, and geogenic) Hg emissions (7400 Mg yr<sup>-1</sup>)<sup>9</sup>. By taking up  
62 Hg, terrestrial ecosystems reduce the burden of Hg depositing in oceans and freshwater  
63 systems, where it can be more readily converted to MeHg and bioaccumulated in fish.  
64 Previous studies have drawn useful analogies between Hg and carbon cycling in  
65 terrestrial ecosystems<sup>10,11</sup>. Like carbon dioxide (CO<sub>2</sub>), elemental mercury (Hg<sup>0</sup>) is  
66 assimilated by foliage throughout the growing season<sup>12</sup>. Mercury is transported from the  
67 canopy to soil by foliage falling to the ground (“litterfall”) and dry deposited Hg being  
68 washed off by precipitation (“throughfall”), which together are the major source (60–  
69 90%) of Hg in soils<sup>8</sup>. Anthropogenic land use and land cover changes (LULCC),  
70 including deforestation, perturb both CO<sub>2</sub> and Hg fluxes to the atmosphere<sup>13–15</sup>. In the

71 case of carbon, scientific assessments<sup>14</sup> have calculated the contribution of LULCC to  
72 total anthropogenic CO<sub>2</sub> emissions (13% of total), and land management practices are  
73 governed by Article 5 of the Paris Agreement<sup>16</sup>. For Hg, on the other hand, quantitative  
74 estimates of the overall importance of land cover change are limited. Only one previous  
75 study modeled the impact of future LULCC on atmospheric Hg cycling, focusing on the  
76 effects of climate-induced changes to vegetation<sup>15</sup>. No anthropogenic Hg emissions  
77 inventories have quantified the impacts of historical and future deforestation, and land  
78 management is not currently addressed by Hg policy efforts like the Minamata  
79 Convention.

80 Several processes mobilize Hg from terrestrial systems after deforestation. Along with  
81 removing a strong atmospheric sink of Hg<sup>8</sup>, deforestation leads to more insolation  
82 reaching the soil, which increases volatilization of Hg from soils through enhanced  
83 microbial<sup>17</sup> or photochemical<sup>18</sup> reduction. Fire-mediated deforestation leads to direct  
84 emission of Hg from forest and soil biomass<sup>19</sup>. Soils in deforested areas are subject to  
85 accelerated erosion rates, enhancing Hg export to downstream ecosystems<sup>17,20,21</sup>. Direct  
86 measurement of deforestation-driven fluxes at larger scales is challenging given  
87 variations in the land sink due to trends in environmental conditions, necessitating the use  
88 of models to quantify these fluxes<sup>22</sup>. Models of terrestrial–atmosphere Hg fluxes, while  
89 still much more uncertain than analogous carbon cycle models, are improving due to a  
90 better process understanding and increasing availability of terrestrial  
91 measurements<sup>8,12,23,24</sup>. Thus, the time is ripe for assessing the relative importance of  
92 deforestation-driven fluxes in the Hg cycle.

93 Policies on local, national, and international scales will shape the future evolution of  
94 deforestation Hg fluxes. Deforestation due to agricultural land conversion threatens the  
95 Amazon rainforest<sup>25,26</sup>, which currently contributes 29% of the global land sink for  
96 atmospheric Hg<sup>0</sup> (ref. <sup>23</sup>). At current deforestation rates, 40% of the Amazon rainforest  
97 could be lost by 2050, while enhanced environmental legislation (e.g., expansion of  
98 protected areas and enforcement) can reduce the deforested area to 15% (ref. <sup>27</sup>).  
99 Reforestation and afforestation on the global scale are being studied as part of the  
100 solution to reach net zero greenhouse gas emissions in the future<sup>28</sup>, though the efficacy of

101 these measures has been debated<sup>29</sup>. In any case, the climate mitigation benefits of  
102 forestation would not be realized without accompanying aggressive CO<sub>2</sub> emissions  
103 reductions<sup>29,30</sup>. Similarly, forest conservation and reforestation policies may have  
104 potential benefits for Hg sequestration on land, yet the magnitude of impacts remain  
105 unquantified.

106 Here, we apply the GEOS-Chem Hg model<sup>23</sup> to calculate deforestation emission factors  
107 for Hg for different regions and evaluate them against available observations. We  
108 quantify the global atmospheric Hg fluxes in 2015 that result from deforestation. We  
109 study the impact of future Amazon deforestation policy scenarios<sup>27</sup> and potential global  
110 reforestation efforts<sup>30</sup> on the terrestrial Hg sink, to investigate the importance of land  
111 management policies for curbing Hg pollution.

## 112 Materials and Methods

113 **Atmospheric Hg model (GEOS-Chem) description.** In this study, we used the chemical-  
114 transport model GEOS-Chem v12.8.1 with Hg<sup>0</sup> dry deposition updates from Feinberg et  
115 al.<sup>23</sup>. The global model was run at 2.0° × 2.5° horizontal resolution and 47 vertical layers  
116 up to 80 km altitude. The model tracks emissions, transport, chemistry, and deposition of  
117 Hg in three chemical tracers: elemental mercury (Hg<sup>0</sup>), oxidized mercury (Hg<sup>II</sup>), and  
118 particulate-bound mercury (Hg<sup>P</sup>). Atmospheric transport of Hg species is based on  
119 MERRA-2 reanalysis meteorological data<sup>31</sup>. The Hg chemical mechanism assumes that  
120 Br is the primary Hg<sup>0</sup> oxidant and uses offline monthly maps of previously-calculated  
121 oxidant concentrations to drive chemistry<sup>32</sup>. The aqueous photoreduction rate of Hg<sup>II</sup> to  
122 Hg<sup>0</sup> is parametrized as a function of the organic aerosol concentration and the NO<sub>2</sub>  
123 photolysis rate<sup>32</sup>.

124 The wet removal of oxidized Hg (Hg<sup>II</sup> and Hg<sup>P</sup>) from the atmosphere is calculated in  
125 online parametrizations considering large-scale and convective scavenging of gas and  
126 particulate species<sup>33</sup>. Dry deposition in GEOS-Chem applies a resistance-based  
127 approach<sup>34</sup>, which determines the dry deposition velocities depending on meteorology  
128 (e.g., temperature and windspeed), land surface parameters (e.g., land type and leaf area  
129 index, LAI), and compound-specific parameters (biological reactivity,  $f_0$ , and solubility,

130  $H^*$ ). For  $Hg^0$ ,  $f_0$  was set to 0.2 within the Amazon rainforest and  $3 \times 10^{-5}$  elsewhere.  
131 These values of  $f_0$  were found to yield the best agreement with available measurements of  
132  $Hg^0$  vegetation uptake<sup>23</sup>, though we later tested the impacts of uncertainties in these  
133 parameters on the modeling results (Section S4). The solubility of  $Hg^0$  is low ( $H^* = 0.11$   
134 M atm<sup>-1</sup>), whereas gaseous  $Hg^{II}$  is assumed to be highly soluble ( $H^* = 10^{14}$  M atm<sup>-1</sup>) and  
135 biologically unreactive ( $f_0 = 0$ ). Dry deposition of  $Hg^P$  is determined according to the  
136 aerosol deposition parametrization in GEOS-Chem<sup>35</sup>. Dry deposition is calculated  
137 separately over each land type within a grid cell (e.g., rainforest, grassland, cropland,  
138 etc.) and then an overall area-weighted average is calculated for the grid cell. GEOS-  
139 Chem accounts for 73 land types based on the Gibbs<sup>36</sup> land cover product. The LAI data  
140 for this study was taken from a reprocessed version of the Moderate Resolution Imaging  
141 Spectroradiometer (MODIS) satellite product<sup>37</sup>.

142 Anthropogenic Hg emissions followed AMAP/UNEP estimates<sup>38</sup> for 2015. Biomass  
143 burning emissions were taken from the Global Fire Emissions Database (GFED) v4.1s<sup>39</sup>.  
144 Fixed concentrations of  $Hg^0$  in the surface ocean based on the MITgcm 3-D ocean  
145 model<sup>32</sup> were used to calculate the  $Hg^0$  air-sea exchange<sup>40</sup>. We adopted a new  
146 formulation<sup>41</sup> for the soil  $Hg^0$  emissions parametrization (Supplementary Information,  
147 Section S1):

$$148 \quad E_{\text{soil}} = aC^bR_g^c \quad (\text{Eq. 1})$$

149 where  $E_{\text{soil}}$  is the  $Hg^0$  emissions from soil (units  $\text{ng m}^{-2} \text{ h}^{-1}$ ),  $C$  is the concentration of Hg  
150 in soils (units  $\mu\text{g g}^{-1}$ ),  $R_g$  is solar radiation flux at the ground (units  $\text{W m}^{-2}$ ), and  $a$ ,  $b$ , and  
151  $c$ , are coefficients (set to 71, 2.5, and 0.76, respectively). The coefficients of this  
152 parametrization were tuned to match available soil emissions measurements (Section S1).  
153 The soil concentration map of Hg ( $C$ ) was calculated using the method of Selin et al.<sup>42</sup>,  
154 deriving the spatial distribution of soil concentrations by first assuming a steady state  
155 balance between land emissions and deposition in the preindustrial and subsequently  
156 increasing soil concentrations according to the distribution of anthropogenic Hg  
157 deposition. As in Selin et al.<sup>42</sup>, the solar radiation at ground ( $R_g$ ) is determined by

158 considering attenuation of the solar radiation flux ( $R_S$ ) by shading from the overhead  
159 canopy, parametrized by the LAI:

160 
$$R_g = R_S \exp\left(-\frac{\alpha \text{LAI}}{\cos\theta}\right) \quad (\text{Eq. 2})$$

161 where  $\alpha = 0.5$ , assuming extinction from a random angular distribution of leaves<sup>43</sup>, and  $\theta$   
162 is the solar zenith angle. Deforestation reduces the leaf area index (LAI) in impacted grid  
163 cells, increasing the solar radiation flux at the ground (Eq. 2) and consequently enhancing  
164 Hg<sup>0</sup> emissions from soils (Eq. 1). We have also updated GEOS-Chem to calculate soil  
165 emissions at the sub-grid scale for each land use category contained within the grid cell.

166 **Reference (HIST) simulation.** We ran a GEOS-Chem simulation for the land cover and  
167 LAI conditions of the year 2003 (HIST simulation), the first year where reprocessed LAI  
168 data is available. To highlight the role of land cover changes alone, meteorological  
169 conditions were kept constant by running all simulations with meteorology for 2014–  
170 2015. We considered the first year as spinup to equilibrate the new land cover conditions,  
171 and analyzed simulation differences for the meteorological year 2015.

172 **Estimating historical global deforestation-driven Hg emissions.** We calculated regional  
173 emissions factors (EFs) for deforestation through conducting perturbation experiments in  
174 GEOS-Chem. Emission factors were distinguished for the following regions based on  
175 biogeographic realms<sup>44</sup>: Palearctic, Nearctic, Afrotropic, Neotropic, Australasia &  
176 Oceania, Indomalaya, China, and the Amazon rainforest (mapped in Fig. S5). We  
177 separated China into its own region as soil Hg concentrations are higher than surrounding  
178 areas due to historical Hg emissions. The Amazon rainforest was separated from other  
179 Neotropic forests due to it having higher observed vegetation uptake fluxes and a  
180 different assigned  $f_0$  parameter in the model dry deposition scheme. For each region, a  
181 simulation was conducted with perturbed land cover in the grid cells that experienced  
182 deforestation during 2000–2014 in the  $0.25^\circ \times 0.25^\circ$  resolution CMIP6 Land-Use  
183 Harmonization (LUH2) dataset<sup>45</sup>. As deforestation is mainly driven by agricultural  
184 expansion<sup>46,47</sup>, we replaced forest land cover in these grid cells with the most common  
185 agricultural land cover relevant to the region: “Crops and Town” (Afrotropic,

186 Indomalaya, Palearctic, Australasia & Oceania, and China), “Corns and Beans  
187 Croplands” (Neotropic and Nearctic), and “Fields and Woody Savannah” (Amazon). For  
188 the new agricultural areas, the LAI was set to the average annual cycle for the existing  
189 agricultural grid cells within the region. Eight deforestation (DFR) simulations (1 for  
190 each region) were conducted for 2014–2015, comparing year 2015 fluxes to the HIST  
191 simulation. To calculate the net emissions factor (EF) from deforestation, we calculated  
192 changes to the land-air exchange over the deforested grid cells:

193 
$$EF = \frac{(E_{DFR} - D_{DFR}) - (E_{HIST} - D_{HIST})}{A_{DFR}} \quad (\text{Eq. 3})$$

194 where  $E$  refers to Hg emissions,  $D$  refers to Hg deposition, and  $A$  refers to the area that is  
195 deforested in the simulation. The emissions factor represents the net emissions of Hg  
196 released by a deforested area annually, in units  $\text{Mg m}^{-2} \text{ yr}^{-1}$ , capturing both the impact of  
197 increased soil  $\text{Hg}^0$  emissions and reduced forest  $\text{Hg}^0$  uptake. The assumption of linearity  
198 of the net emissions to deforested area holds in simulations conducted in the Amazon  
199 with differing spatial distributions of deforestation (Fig. S4), supporting an emissions  
200 factor approach to deforestation. We compared calculated emissions factors with existing  
201 estimates from observational studies<sup>18,21,24,48–64</sup> for total deforestation EFs and the  
202 component of EFs due to soil  $\text{Hg}^0$  emissions (Supplementary Information, Section S2).  
203 Based on our literature review (SI Spreadsheet), observational data is available for three  
204 of the tested regions (Amazon, China, and Nearctic).

205 We applied the regional emissions factor to historical land use data from the LUH2  
206 dataset to calculate emissions from deforestation. We defined gross deforested areas from  
207 the LUH2 dataset by summing the areas with transitions from primary or secondary  
208 forest to a non-forest land type. This approach does not consider LULCC fluxes due to  
209 harvesting of a forest without complete deforestation or the regrowth of vegetation after  
210 clearing, due to a lack of corresponding observations for Hg to constrain these  
211 parameters. Likewise, the emissions factors were assumed to be constant annually, so a  
212 deforested area continues to have the same total emissions for each year over the  
213 considered time horizon. In reality, deforested areas could have a recovery timescale as  
214 vegetation regrows, which is accounted for in carbon LULCC fluxes<sup>65</sup>; for Hg, the

215 response timescales during regrowth are largely unknown. To account for these  
216 uncertainties, we produced global and country-level estimates of Hg emissions in 2015  
217 due to deforestation by summing deforestation over different time horizons: 15 years  
218 (2000–2014), 30 years (1985–2014), 45 years (1970–2014), and 60 years (1955–2014).  
219 The 45-year (1970–2014) accumulated results are presented in the main text, with the  
220 others presented in Fig. S6.

221 **Future Amazon deforestation scenarios.** We employed deforestation scenarios from  
222 Soares-Filho et al.<sup>27</sup>, who developed a model for predicting the extent of deforestation  
223 within the Amazon based on environmental policies and highway construction. They  
224 presented two scenarios for 2050, encompassing a range of future deforestation  
225 trajectories. In the Business as Usual (BAU) scenario, recent deforestation trends  
226 continue into the future, assuming that compliance with conservation laws remains low  
227 and no new areas will be protected. On the other hand, the Governance (GOV) scenario  
228 assumes that the expansion of environmental legislation and increased enforcement of  
229 protected areas will lead to a reduction in the deforestation rate. Compared to the  
230 Amazon forest area in 2003 (5.3 million km<sup>2</sup>), in 2050 the BAU scenario projects 3.2  
231 million km<sup>2</sup> remaining and GOV projects 4.5 million km<sup>2</sup> remaining<sup>27</sup>. We focused our  
232 analysis on comparing the forest coverage in the years 2003 and 2050.

233 We translated these scenarios into required inputs for the calculations in GEOS-Chem  
234 (spatially gridded land use categories, LAI, and biomass burning emissions). The Soares-  
235 Filho et al.<sup>27</sup> dataset assigns 1 km<sup>2</sup> pixels within the Amazon basin as being forested,  
236 deforested, or agricultural areas for every year between 2003 and 2050. These annual  
237 datasets were regridded to 0.25° × 0.25° resolution, the native resolution of land use and  
238 LAI maps in GEOS-Chem. We calculated the relative change in forested area in the  
239 scenarios for every 0.25° × 0.25° grid cell. The rainforest land use category in deforested  
240 grid cells was correspondingly reduced by this factor, with the lost land area added to the  
241 land use category for “Fields and Woody Savanna”. The LAI annual cycle for existing  
242 Fields and Woody Savanna grid cells within the Amazon basin was spatially averaged  
243 over 2003 and assigned to the deforested areas. Annual average LAI maps for the  
244 Amazon scenarios used in GEOS-Chem are shown in Fig. S9. For these simulations, we

245 assumed that conversion of forest to agricultural land within the Amazon is fire-  
246 mediated<sup>66</sup>. Gridded biomass burning emissions were calculated by multiplying the  
247 newly deforested areas for each year by mean fire Hg emissions ( $380 \mu\text{g m}^{-2} \text{ yr}^{-1}$ ) from  
248 two observational studies in the Amazon<sup>19,67</sup>. An additional 50% of the emissions (190  
249  $\mu\text{g m}^{-2} \text{ yr}^{-1}$ ) are released to the atmosphere within the first year as post-burn Hg<sup>0</sup>  
250 emissions from soils<sup>18</sup>. To account for seasonal differences in meteorology and realistic  
251 timing for forest clearing and burning<sup>66</sup>, we assumed that deforestation occurs at the start  
252 of June and deforestation biomass burning emissions occur in August and September .

253 The BAU and GOV scenarios do not account for any land-climate feedbacks<sup>27</sup>, wherein  
254 deforestation of the rainforest can lead to reduced moisture recycling and widespread  
255 *savannization* (conversion of rainforest to savanna)<sup>68</sup>. As an upper bound for this process,  
256 we considered an extreme scenario (SAV) where the Amazon rainforest is fully  
257 converted to savanna<sup>69</sup>. The impact of this scenario on Hg<sup>0</sup> deposition was previously  
258 quantified<sup>23</sup>, but here we reran the SAV simulation in GEOS-Chem to account for  
259 updates in the soil Hg<sup>0</sup> emissions parametrization. Fluxes for the Amazon region were  
260 calculated by averaging over the area covered by the Soares-Filho et al.<sup>27</sup> deforestation  
261 projections (shown in Fig. S8).

262 **Potential reforestation scenario.** We applied a reforestation scenario (RFR) in GEOS-  
263 Chem based on the Global Reforestation Potential map<sup>30,70</sup>, which considers the binary  
264 potential of every 1 km<sup>2</sup> grid cell to be converted from non-forest (<25% tree cover in  
265 2000–2009) to forest (>25% tree cover). The reforestation potential dataset does not  
266 include areas that are native non-forest land cover types (e.g., grasslands) or cropland  
267 areas. The reforestation potential was regredded to  $0.25^\circ \times 0.25^\circ$  resolution. For every  
268 grid cell where reforestation can occur, we identified the corresponding biome in the  
269 Ecoregions2017 dataset<sup>44</sup> to determine the type of native forest vegetation that would  
270 occur. If the corresponding biome of the grid cell was not a forest (e.g., coastal grid  
271 cells), the most common forest type in the 8 neighboring grid cells was selected. The  
272 added forest was assumed to have a LAI annual cycle equal to the 2003 spatial average  
273 for all grid cells in the corresponding biome and biogeographic realm (LAI<sub>biome</sub>). For grid  
274 cells that were not a forest land type in 2003, we converted the reforested area fraction

275 ( $f_{\text{rfr}}$ ) from the original land type to the new forest land type. Only grid cells where  
276  $\text{LAI}_{\text{biome}}$  is larger than the original land type LAI ( $\text{LAI}_{\text{old}}$ ) were reforested. Since the land  
277 map used in GEOS-Chem is at coarser resolution ( $0.25^{\circ} \times 0.25^{\circ}$ ) than the reforestation  
278 potential dataset ( $1 \text{ km} \times 1 \text{ km}$ ), the reforested grid cell may already be a forest land type  
279 in GEOS-Chem. In this case, we assumed that the grid cell LAI ( $\text{LAI}_{\text{new}}$ ) will become  
280 denser due to the new reforested area:

281 
$$\text{LAI}_{\text{new}} = \text{LAI}_{\text{old}} + f_{\text{rfr}} \cdot \text{LAI}_{\text{biome}} \quad (\text{Eq. 4})$$

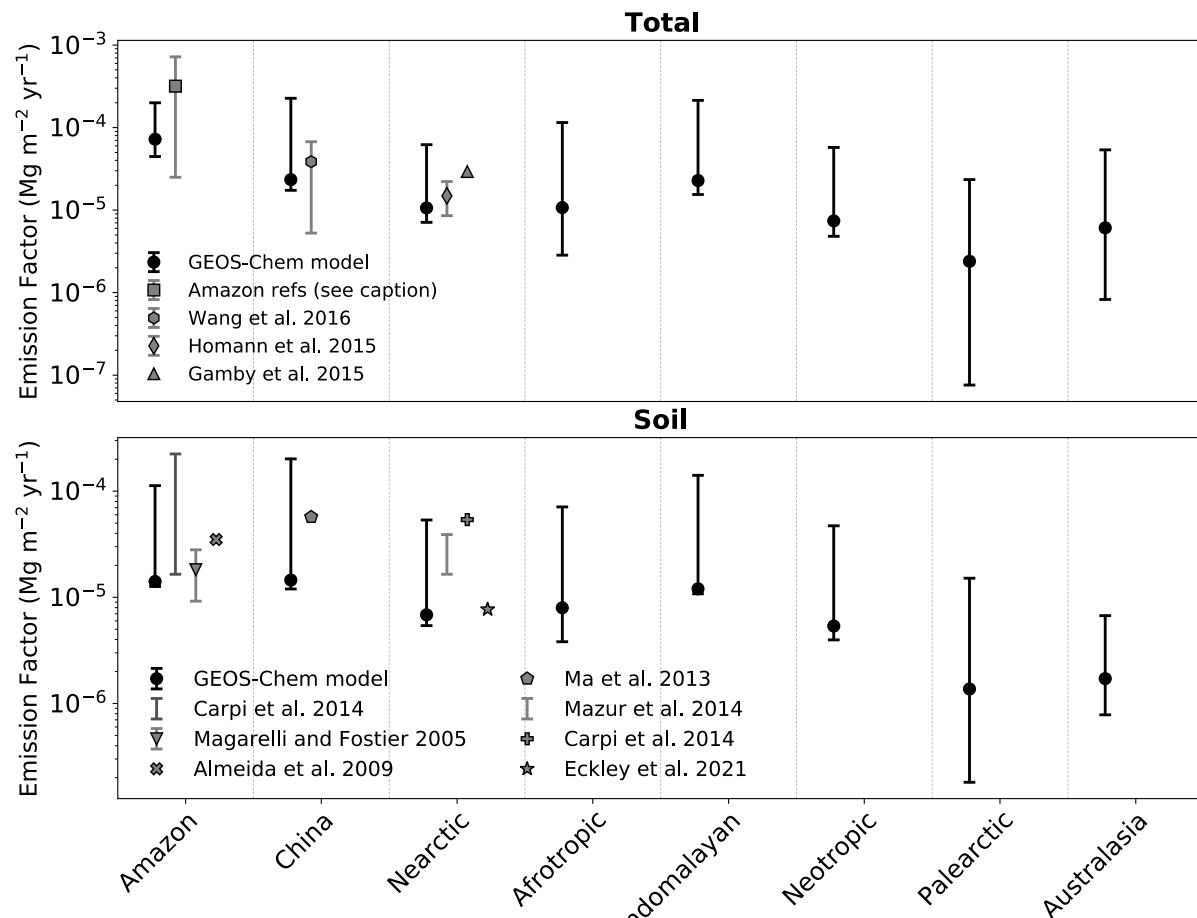
282 The resultant average LAI map in the RFR scenario is shown in Fig. S10.

283 **Uncertainty analysis.** We employed offline Python-based models for  $\text{Hg}^0$  dry deposition  
284 and soil  $\text{Hg}^0$  emissions to estimate uncertainties in the simulated terrestrial-atmosphere  
285  $\text{Hg}$  fluxes from GEOS-Chem. These models are made publicly available for further reuse  
286 (see Code and Data Availability). We focused on offline modeling of the  $\text{Hg}^0$  dry  
287 deposition and soil emissions as these processes contribute the overwhelming majority  
288 ( $>98\%$ ) of the flux response to deforestation. The offline models contain the stand-alone  
289 GEOS-Chem code for calculation of dry deposition velocities and soil emissions across  
290 the horizontal model grid, but do not calculate atmospheric transport or chemical  
291 transformations. Dry deposition fluxes of  $\text{Hg}^0$  were calculated by multiplying the  
292 deposition velocities by previously computed monthly  $\text{Hg}^0$  concentration fields from the  
293 online simulations. The offline models were run for the year 2015 using monthly average  
294 diurnal cycles ( $12 \times 24 \text{ h} = 288$  timesteps) of meteorological parameters, land surface  
295 parameters, and  $\text{Hg}^0$  concentration fields. At this time resolution, the offline models  
296 showed sufficient accuracy compared to full online GEOS-Chem simulations, with  
297 maximum errors compared to online predictions of 1% for annual mean soil emissions  
298 and 5% for  $\text{Hg}^0$  deposition. Given this level of accuracy and reduced computational  
299 expense, the offline models are appropriate for estimating the parametric uncertainties in  
300 atmosphere-terrestrial fluxes of the online GEOS-Chem model. We considered the  
301 contributions of deposition parameters ( $f_0$ ), soil emission parametrizations, the  
302 assumption for LAI for replaced land types, and biomass burning emission factors (for  
303 the Amazon simulations) to the overall uncertainty in fluxes. Uncertainty bounds of these

304 parameters are tabulated in Table S4. Latin Hypercube sampling<sup>71</sup> was used to sample  
305 100 parameter combinations. We conducted 100 simulations in the offline emissions and  
306 deposition models for each studied scenario, calculating 95% confidence intervals from  
307 the 2.5<sup>th</sup> and 97.5<sup>th</sup> percentile values in the offline calculated fluxes.

308 **Results and Discussion**

309 ***Global estimate of deforestation-driven Hg fluxes.*** To calculate net deforestation  
310 emissions, we computed the difference in the net terrestrial-atmosphere exchange  
311 (emissions from a grid cell minus deposition to a grid cell) before and after deforestation  
312 (Eq. 3). For our global estimate of deforestation-driven emissions, we did not consider  
313 immediate biomass burning emissions of Hg due to fire-mediated forest clearing nor  
314 enhanced erosion fluxes, instead focusing on the impact on net Hg fluxes to the  
315 atmosphere in the years after the clearing event. The major impacts to Hg fluxes arise  
316 through enhanced soil Hg<sup>0</sup> emissions and decreased Hg<sup>0</sup> dry deposition due to reduced  
317 canopy coverage, which can continue many years after the initial deforestation event<sup>18,61</sup>.  
318 Using perturbation simulations in GEOS-Chem for 8 global land regions, we calculated  
319 regional emission factors (EFs) representing net fluxes to the atmosphere per unit  
320 deforested area (in units Mg Hg m<sup>-2</sup> yr<sup>-1</sup>).



321

322 **Figure 1.** Comparison between modeled and observation-derived net emission factors (EFs) for  
 323 deforestation in different regions. The upper panel shows total EFs and the lower panel shows the  
 324 soil  $\text{Hg}^0$  emissions component of deforestation EFs. Modeled circles show the best estimate  
 325 (online simulations), while error bars show the 95% confidence interval due to model parameter  
 326 uncertainties (calculated in offline simulations, Section S4). Observation estimates are from  
 327 refs.<sup>18,21,24,48–64</sup>, with the Amazon Total EF estimate based on measurements in Fig. S3. Observed  
 328 error bars refer to uncertainty ranges when multiple plots were measured within a study (further  
 329 information about these calculations can be found in Section S2 and the SI Spreadsheets).

330

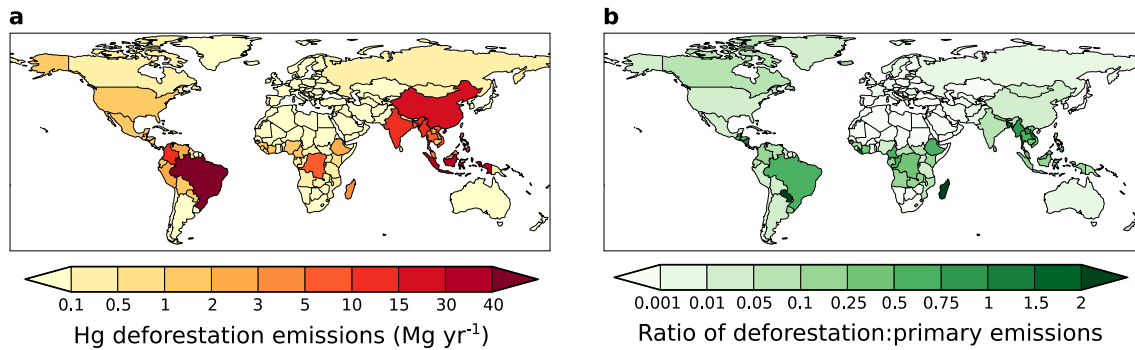
331 The calculated EFs are on the order of  $10^{-6}$  to  $10^{-4}$   $\text{Mg Hg m}^{-2} \text{ yr}^{-1}$  depending on the  
 332 region (Fig. 1; Table S3), with the Amazon rainforest showing the highest EF ( $7 \times 10^{-4}$   
 333  $\text{Mg Hg m}^{-2} \text{ yr}^{-1}$ ; 95% confidence interval, CI:  $4 \times 10^{-5}$  to  $2 \times 10^{-4}$   $\text{Mg Hg m}^{-2} \text{ yr}^{-1}$ ). This is  
 334 to be expected from litterfall and throughfall measurements in the Amazon, which show  
 335 some of the highest levels of  $\text{Hg}^0$  vegetation uptake observed globally<sup>13</sup>, as well as  $\text{Hg}^0$   
 336 soil flux measurements from deforested areas in the Amazon, which show higher levels

337 of emissions compared to deforested North American soils<sup>18</sup>. The variation of simulated  
338 EFs between regions depend on the factors that affect dry deposition (vegetation type and  
339 LAI) and soil emission fluxes (LAI, soil Hg concentrations, and solar radiation). We  
340 compiled available estimates of deforestation EFs from previous observational  
341 studies<sup>18,21,24,48–64</sup> and compared these to our modeled values (Fig. 1). Our EFs overlap  
342 with available factors derived from observations, for the three regions where data are  
343 available. The modeled error ranges appear well-calibrated as they cover a similar range  
344 as the variability between observation-derived fluxes in the same region (Fig. 1). Fig. 1  
345 also highlights that no observations of the impact of deforestation on Hg cycling are  
346 currently available from the Afrotropic and Indomalayan regions, where deforestation is  
347 widespread.

348 We multiplied the regional EFs by the deforested area from the CMIP6 Land-Use  
349 Harmonization (LUH2) dataset<sup>45</sup> to calculate the net Hg fluxes to the atmosphere from  
350 deforestation. Given the uncertain timescale for recovery in Hg sink capacity after  
351 deforestation, we assumed that a deforested area has constant annual emissions over a  
352 considered time horizon. Previous LULCC studies for carbon suggest that forests recover  
353 their original biomass within 75 years after deforestation<sup>65</sup>, so we employed time  
354 horizons between 15–60 years (Fig. S6) to calculate 2015 deforestation-driven emissions.  
355 In Fig. 2a, country-level deforestation emissions are shown based on a 45-year time  
356 horizon (emissions released from areas deforested between 1970 and 2014). Net  
357 emissions occurring in 2015 considering this 45-year deforestation time horizon are 217  
358 Mg yr<sup>-1</sup> globally (CI: 134–1650 Mg yr<sup>-1</sup>). Countries with substantial (>10 Mg yr<sup>-1</sup>)  
359 deforestation-driven emissions include Brazil (43 Mg yr<sup>-1</sup>), Indonesia (35 Mg yr<sup>-1</sup>), China  
360 (16 Mg yr<sup>-1</sup>), Colombia (14 Mg yr<sup>-1</sup>), India (13 Mg yr<sup>-1</sup>), Philippines (11 Mg yr<sup>-1</sup>), and  
361 Myanmar (11 Mg yr<sup>-1</sup>). To put these emissions into context, Fig. 2b compares the  
362 deforestation emissions with 2015 primary anthropogenic emissions inventory from  
363 AMAP/UNEP<sup>9,38</sup>. Deforestation Hg emissions are minor (<5%) compared to primary  
364 anthropogenic emissions for most countries. However, for 32 countries, all located in the  
365 tropics, deforestation emissions are greater than 30% of primary emissions. For Brazil,  
366 which is the fifth highest emitter of primary Hg<sup>9,38</sup>, deforestation emissions (43 Mg yr<sup>-1</sup>)

367 are only 40% smaller than the 2015 emissions from primary anthropogenic sources (71  
 368 Mg  $\text{yr}^{-1}$ ). Deforestation emissions even exceed primary emissions in some countries,  
 369 including Madagascar (deforestation emissions are 2.4 $\times$  larger), Paraguay (2.3 $\times$ ), Liberia  
 370 (2.0 $\times$ ), and Bangladesh (1.8 $\times$ ). Currently, Hg emissions inventories<sup>9</sup> only consider  
 371 primary anthropogenic emissions (2222 Mg  $\text{yr}^{-1}$  in 2015), overlooking deforestation as a  
 372 significant source of anthropogenic Hg to the atmosphere (217 Mg  $\text{yr}^{-1}$ ). The relative  
 373 importance of deforestation as an anthropogenic driver of Hg pollution could increase  
 374 over the next decades, with primary anthropogenic emissions of Hg projected to halve to  
 375 1020 Mg  $\text{yr}^{-1}$  by 2035 under Minamata policies and reductions in fossil fuel use<sup>72</sup>.  
 376 Therefore, assessing the potential impacts of land use policy scenarios will be crucial for  
 377 predicting future Hg cycling, as primary anthropogenic emissions decline in the future.

378



379

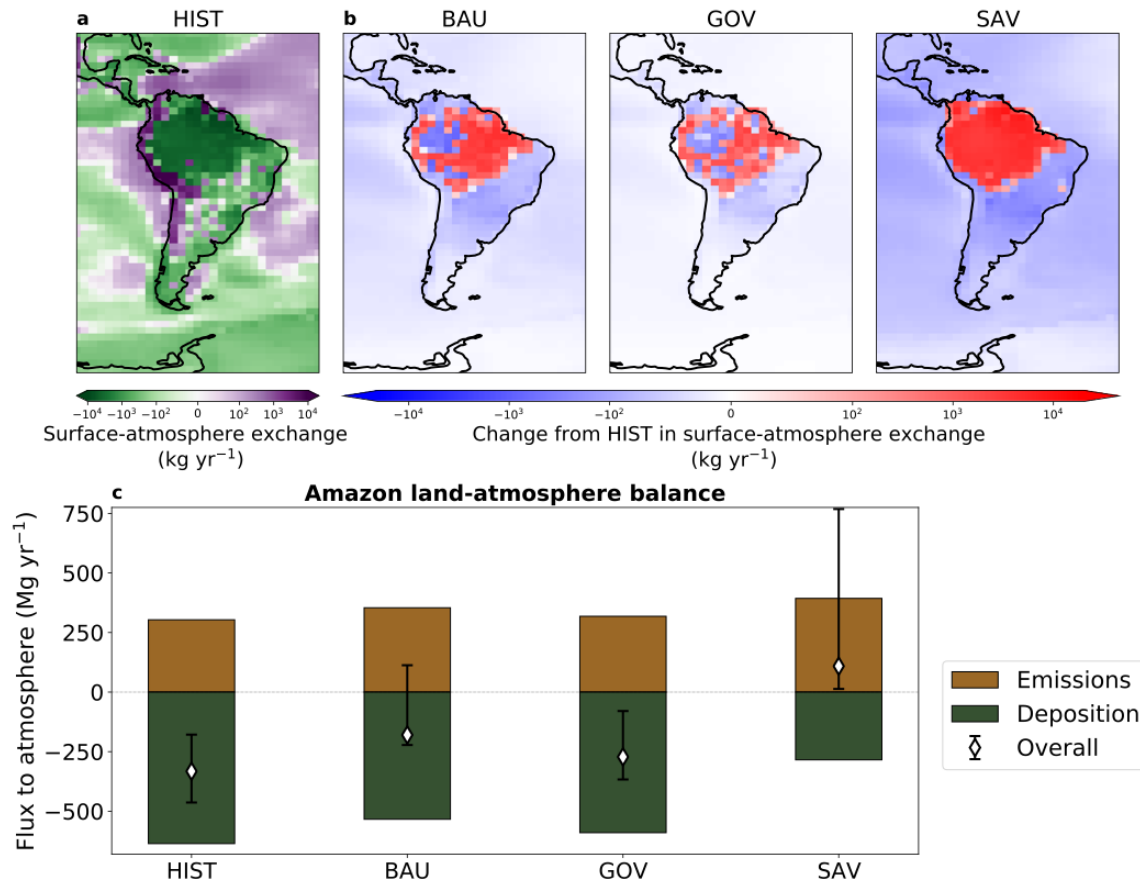
380 **Figure 2.** Country-level annual deforestation emissions of Hg in 2015. (a) Deforestation-driven  
 381 net emissions of Hg by country, assuming that deforested areas from the previous 45 years  
 382 (1970–2014) contribute to emissions. (b) Ratio of deforestation emissions to primary  
 383 anthropogenic emissions<sup>9,38</sup> by country.

384

385 **Amazon conservation policy impacts on Hg cycling.** The Amazon is one of the regions  
 386 with the highest Hg fluxes from deforestation (Fig. 2) and land policy choices will  
 387 determine how this evolves in the future. Under historical forest coverage from 2003  
 388 (HIST simulation), the Amazon rainforest stands out as a strong global sink of Hg (Fig.  
 389 3a), with net input from the atmosphere to the rainforest totaling 332 Mg  $\text{yr}^{-1}$  (CI: 179–  
 390 463 Mg  $\text{yr}^{-1}$ ). We studied the evolution of the Amazon Hg sink in two deforestation  
 391 scenarios<sup>27</sup> for 2050: a business-as-usual scenario (BAU), which extrapolates historical  
 392 deforestation tendencies into the future, and a governance scenario (GOV), which

393 assumes expanded conservation of the rainforest in the future. In the BAU scenario,  
394 widespread deforestation, mainly in eastern Amazonia, reduces the net Hg inputs to soils  
395 (Fig. 3b). While the Amazon region overall remains a net Hg sink in BAU, the removed  
396 vegetation leads to decreased Hg<sup>0</sup> deposition in the Amazon (change from HIST: -105  
397 Mg yr<sup>-1</sup>; CI: -53 to -152 Mg yr<sup>-1</sup>) and enhanced Hg<sup>0</sup> emissions from soils (+35 Mg yr<sup>-1</sup> ;  
398 CI: 28–275 Mg yr<sup>-1</sup>). For the Amazon policy scenarios, we have also considered the  
399 impact that fire-mediated forest clearing<sup>66,73</sup> has on biomass burning emissions of Hg,  
400 which are 15 Mg yr<sup>-1</sup> (CI: 10–17 Mg yr<sup>-1</sup>) larger in BAU than HIST. The BAU scenario  
401 shows atmospheric Hg<sup>0</sup> concentrations increasing up to 0.3 ng m<sup>-3</sup> (+50%) within the  
402 Amazon region (Fig. S11); this would be a detectable change in Hg<sup>0</sup>, comparable to the  
403 0.5 ng m<sup>-3</sup> (-30%) decrease between 1995–2015 in North American Hg<sup>0</sup> observations<sup>74</sup>.  
404 The additional Hg fluxes from deforested areas can be transported over long distances in  
405 the atmosphere and lead to more Hg deposition over oceans and remaining intact forest  
406 areas (Fig. 3b). In the GOV scenario, deforestation is slowed by the conservation  
407 measures, leading to smaller perturbations in the dry deposition flux from HIST (-47 Mg  
408 yr<sup>-1</sup> ; CI: -25 to -68 Mg yr<sup>-1</sup>) and the soil emission flux (+16 Mg yr<sup>-1</sup>; CI: 12–126 Mg yr<sup>-1</sup>)  
409 (Fig. 3b). In GOV, burning emissions from deforestation are 1 Mg yr<sup>-1</sup> lower than in  
410 HIST, due to lower annual rates of deforestation in the 2050 GOV scenario compared to  
411 the HIST case representing 2003. Globally, the weakened rainforest sink of Hg yields  
412 higher deposition of Hg to oceans compared to the reference simulation (BAU – HIST =  
413 +108 Mg yr<sup>-1</sup>; GOV – HIST = +44 Mg yr<sup>-1</sup>).

414 Deforestation can be exacerbated through climate feedbacks, which are not considered in  
415 these policy scenarios. For example, BAU projects that 40% of the Amazon will be  
416 deforested by 2050<sup>27</sup>, which could trigger a tipping point with widespread transition of  
417 the rainforest to a savannah biome under diminished regional moisture recycling<sup>68</sup>. To  
418 evaluate this, we also re-ran an upper limit scenario from our previous work<sup>23</sup> where the  
419 entire rainforest is converted to savannah (SAV). In this case, a strong decline in Hg<sup>0</sup> dry  
420 deposition (-359 Mg yr<sup>-1</sup>; CI: -210 to -503 Mg yr<sup>-1</sup>) and an increase in Hg<sup>0</sup> soil emissions  
421 (+89 Mg yr<sup>-1</sup>; CI: 68 to 652 Mg yr<sup>-1</sup>) drive enhanced inputs of Hg to the ocean (343 Mg  
422 yr<sup>-1</sup>) (Fig. 3b).



423

424 **Figure 3.** Impacts of Amazon deforestation scenarios on surface-atmosphere Hg exchange. (a) The simulated surface-atmosphere exchange (net deposition is negative and net emission is positive) of Hg in the reference simulation (HIST). (b) Changes in exchange fluxes from HIST are shown for the deforestation scenarios: Business-as-usual (BAU), Governance (GOV), and Savannization (SAV); negative values refer to increased net fluxes to the surface compared to HIST and positive values refer to increased net fluxes to the atmosphere. (c) Total simulated fluxes of Hg emissions and deposition are calculated for the Amazon region in each scenario. White diamonds illustrate the net flux of Hg to the atmosphere (= emissions – deposition) and error bars refer to the 95% confidence interval based on model parameter uncertainties.

433

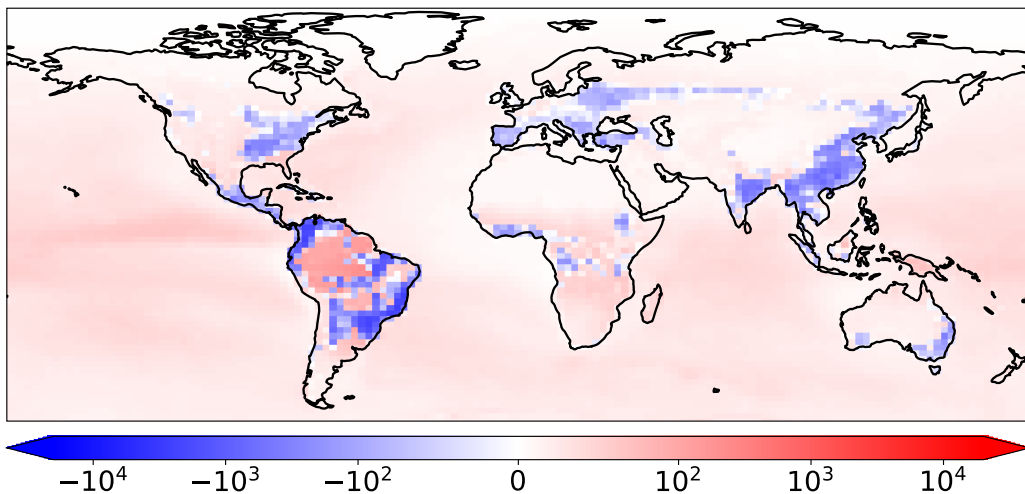
434 This change in the fate of atmospheric Hg (deposition to ocean instead of land) affects  
 435 both the spatial distribution and bioavailability of Hg pollution. When sequestered in  
 436 soils, Hg has an estimated residence time on the order of hundreds of years, whereas in  
 437 the surface ocean Hg is recycled to the atmosphere within months to years<sup>7,11</sup>.  
 438 Deforestation thus increases the mobility of Hg by transferring Hg from locally-  
 439 sequestered reservoirs to the global pool. Human health risks are driven by exposure to  
 440 the more toxic form of the element, MeHg, which is produced through methylation in the

441 environment<sup>2,75</sup>. Deforestation shifts Hg inputs from land to the ocean, where Hg can  
442 more readily be methylated and bioaccumulate to dangerous levels in commercial fish.  
443 Methylation and bioaccumulation of Hg can also occur in forested soils, but MeHg levels  
444 in aquatic ecosystems are generally much higher (overall global ocean average = 15%)<sup>76</sup>  
445 than in Amazonian soils (1–5%)<sup>48,77</sup>. In addition, the long length of aquatic food chains  
446 leads to high levels of MeHg in commonly consumed fish species at higher trophic levels  
447 (e.g., tuna, cod, and swordfish)<sup>75</sup>.

448 Deforestation policy substantially impacts the soil mass balance of Hg in the Amazon  
449 region, illustrated by our modeling simulations (Fig. 3c) and available field observations  
450 (Fig. S3). If agricultural expansion continues as in BAU, the net Amazon sink of  
451 atmospheric Hg is weakened by 153 Mg yr<sup>-1</sup> (CI: 97–418 Mg yr<sup>-1</sup>) (Fig. 3c). The  
452 reduction of forest Hg<sup>0</sup> uptake contributes two-thirds of the net flux response in the BAU  
453 scenario, while increases in emissions contribute the remaining third. Under the more  
454 moderate GOV scenario, the Amazon Hg sink (272 Mg yr<sup>-1</sup>; CI: 79–367 Mg yr<sup>-1</sup>) is better  
455 preserved, though still 18% (CI: 14–65%) smaller than HIST. Stricter conservation  
456 policies in GOV yield an additional 92 Mg yr<sup>-1</sup> (CI: 59–234 Mg yr<sup>-1</sup>) of Hg sequestered in  
457 the Amazon compared to BAU. The SAV scenario illustrates that additional climate  
458 feedbacks could flip the Amazon from a net Hg sink to a source (+109 Mg yr<sup>-1</sup>; CI: 13–  
459 768 Mg yr<sup>-1</sup>). These Hg projections parallel recent findings on Amazon carbon cycling,  
460 which have demonstrated that climate change and deforestation are turning the Amazon  
461 into a CO<sub>2</sub> source<sup>25</sup>. In addition to atmosphere-terrestrial exchange fluxes, soil erosion of  
462 Hg can also be altered due to deforestation. We applied a soil erosion model GloSEM<sup>78,79</sup>  
463 to evaluate the impact of deforestation on erosion in the Amazon basin (Supplementary  
464 Information Section S6). In terms of Hg flux magnitudes, perturbations to erosion are  
465 smaller (<15%) than changes to the atmosphere-terrestrial exchange fluxes (Section S6),  
466 which is supported by field studies<sup>64</sup>. Nevertheless, deforestation also enhances Hg  
467 erosion in both scenarios (BAU: +33%; GOV: +14%), accelerating the transfer of  
468 terrestrial Hg to aquatic ecosystems.

469 ***Quantifying the Hg mitigation potential of reforestation.*** Reforestation has been  
470 identified as a potential mitigation approach for climate change, by strengthening the

471 terrestrial CO<sub>2</sub> sink<sup>30,80</sup>. To investigate the concurrent strengthening of the terrestrial Hg  
 472 sink and the impacts on Hg cycling, we considered a global reforestation scenario (RFR)  
 473 based on the Global Reforestation Potential Map<sup>30,70</sup>, which identified areas suitable for  
 474 reforestation worldwide (i.e., not including croplands or areas where forests are not  
 475 native). Figure 4 maps the impacts of reforestation on Hg surface-atmosphere exchange,  
 476 comparing to the reference HIST simulation. The spatial distribution of reforestation  
 477 impacts depends both on the areal extent of reforestation as well as the reforested  
 478 vegetation type. Net deposition of Hg increases over reforested areas (blue areas in Fig.  
 479 4), while net deposition declines over the ocean as well as land areas with existing forests  
 480 (red areas in Fig. 4). Globally, RFR enhances uptake of Hg on land by 98 Mg yr<sup>-1</sup> (CI:  
 481 64–449 Mg yr<sup>-1</sup>) compared to HIST, thereby reducing Hg deposition to oceans.  
 482 Reforestation could thus take up approximately 5% of the anthropogenic Hg emission  
 483 flux (~2200 Mg yr<sup>-1</sup>)<sup>9</sup>. In addition to the targeted benefits for biodiversity and climate  
 484 change mitigation<sup>30</sup>, reforestation could moderately reduce levels of Hg in marine  
 485 ecosystems, and thus commercial fish. Nevertheless, the magnitude of reforestation  
 486 impact (5% of primary emissions) illustrates that reforestation is not a substitute for  
 487 implementing extensive cuts to primary Hg emissions, like in the CO<sub>2</sub> context<sup>29</sup>.



488  
 489 **Figure 4.** Enhanced land sink of Hg with reforestation. The impact of the potential reforestation  
 490 (RFR) scenario on surface-atmosphere exchange. The differences from the reference (HIST)  
 491 simulation are shown, with negative values referring to increased net fluxes to the surface and  
 492 positive values referring to decreased net fluxes to the surface.

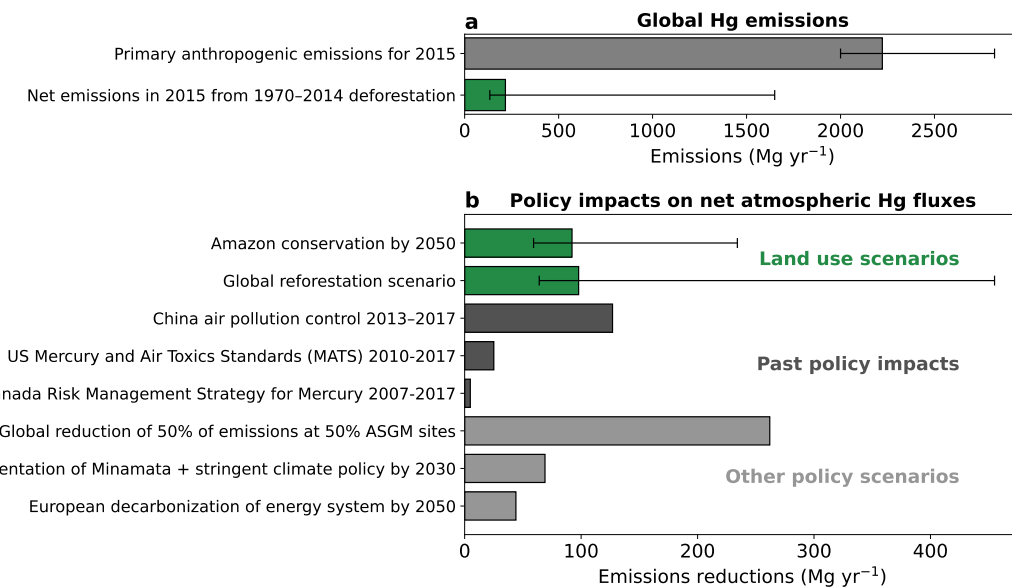
493 Potential reforestation opportunities for Hg are dominated by the Amazon and Atlantic  
494 forest regions in South America ( $71 \text{ Mg yr}^{-1}$ , 72% of total land sink impact) (Fig. 4). The  
495 potential reforestation impact on atmospheric fluxes in Northern extratropical areas alone  
496 ( $-29 \text{ Mg yr}^{-1}$ ) would not compensate for increased Hg emissions due to deforestation in  
497 the Amazon (BAU:  $+153 \text{ Mg yr}^{-1}$ ; GOV:  $+61 \text{ Mg yr}^{-1}$ ). Overall, more information would  
498 be needed to compare the potentials of reforestation and conservation policies on a global  
499 scale, as the deforestation policy scenarios focused only on a specific region (the  
500 Amazon); future research could study conservation impacts in other tropical regions with  
501 high Hg deforestation emissions (Fig. 2) (e.g., in Africa and Southeast Asia). Our  
502 simulated fluxes consider the uptake of Hg upon maturation of forest stands, as reforested  
503 areas are assumed to have LAI of existent corresponding biomes. Further experimental  
504 research would be required to understand the transient response of Hg uptake during the  
505 growth of forests.

506 ***Limitations of modeling approach.*** The current work provides an initial assessment of  
507 the global emissions of Hg from deforestation, which can spur future investigation into  
508 the impact of LULCC on Hg. Other LULCC processes (e.g., wood harvest and  
509 agricultural practices) may also affect Hg fluxes but have not been considered within this  
510 study. As well, due to the early stage of Hg research, there is not yet the same level of  
511 information for Hg that is commonly included in LULCC assessments for carbon,  
512 including temporal information on the release of Hg from soils and Hg uptake rates  
513 during regrowth of vegetation<sup>22</sup>. Although we have assembled a dataset of available  
514 deforestation flux measurements covering multiple regions (SI Spreadsheet), there  
515 continues to be a lack of measurements in relevant regions (e.g., Afrotropic and  
516 Indomalayan) to constrain the response of Hg fluxes to deforestation, contributing  
517 uncertainty to this work. As information from field measurements becomes more  
518 available, it will be possible for future modeling studies to analyze smaller sub-regions  
519 differentiated by ecosystem types, improving the accuracy of deforestation-driven  
520 emissions. In the current work, the parametrization of  $\text{Hg}^0$  soil emissions is based on  
521 solar radiation and soil Hg concentration, which is the current state of the art for global  
522 models and in agreement with available flux measurements (Fig. 1). Field

523 observations<sup>81,82</sup> have investigated the role of other environmental parameters including  
524 precipitation, soil moisture, soil chemistry, soil physics, and microbial interactions, along  
525 with anthropogenic factors such as emissions from directly contaminated soils<sup>83</sup> that  
526 would not be captured at the resolution of the global modeling approach. Regional  
527 models of Hg<sup>0</sup> soil emissions include a wider array of these parameters<sup>24</sup>, but further  
528 research would be required to produce a tuned parametrization of this complexity at the  
529 global scale. The development of terrestrial Hg cycles and LULCC processes within  
530 Earth system models<sup>84</sup> will be vital to investigate the evolution of the Hg land sink over  
531 time and the effect on environmental Hg risks.

532 **Implications for global Hg policy.** Land use policy has been largely unexplored as a  
533 lever to mitigate Hg pollution. On the global scale, the estimated deforestation-driven Hg  
534 emissions in 2015 (217 Mg yr<sup>-1</sup>; CI: 134–1650 Mg yr<sup>-1</sup>) correspond to 10% of the global  
535 primary anthropogenic emissions<sup>9</sup> (2222 Mg yr<sup>-1</sup>) (Fig. 5a). Therefore, though cutting  
536 primary anthropogenic emissions remains a priority, deforestation fluxes should not be  
537 overlooked in assessments of Hg pollution, especially for countries in the tropics (Fig.  
538 2b). The potential of Amazon conservation and global reforestation to reduce net Hg  
539 emissions in the future is substantial compared to previously quantified policies aimed at  
540 tackling primary anthropogenic emissions (Fig. 5b). Potential emissions reductions from  
541 Amazon conservation (92 Mg yr<sup>-1</sup>) and global reforestation (98 Mg yr<sup>-1</sup>) are within the  
542 range of impacts of past policy and future policy scenarios aimed at reducing Hg from  
543 specific anthropogenic sources or due to national climate and air pollution policies (5–  
544 262 Mg yr<sup>-1</sup>)<sup>85–90</sup>. Emissions reductions from land use policies are different from primary  
545 emissions reductions in that their efficacy depends on whether the storage of Hg in soils  
546 is over a long-term period. Similar to CO<sub>2</sub>, the potential benefits of enhanced Hg uptake  
547 on land can be reversed by human or natural disturbances, e.g., by climate change  
548 increasing the frequency of wildfires — which re-emit Hg and carbon from terrestrial  
549 ecosystems — and droughts — which reduce Hg and CO<sub>2</sub> uptake by plants<sup>30,91</sup>. Thus,  
550 mitigation of Hg pollution by conserving and increasing forest area can only be realized  
551 with concurrent efforts to sustainably manage land areas and preventing severe climate  
552 change. The potential of sustainable land use to mitigate Hg pollution could enable

553 collaborations between the Minamata Convention and other global policy efforts to  
 554 reduce deforestation, e.g., the 2021 Glasgow Declaration<sup>92</sup>. Ultimately, mitigation of  
 555 global Hg pollution depends not only on reducing primary anthropogenic emissions, but  
 556 also reducing anthropogenic activities like deforestation that re-mobilize legacy Hg.



557  
 558 **Figure 5.** Potential of land use policies to reduce net Hg fluxes to the atmosphere. (a) Comparing  
 559 global 2015 emissions from primary anthropogenic emissions<sup>9,38</sup> and deforestation-driven  
 560 emissions, assuming a 45-year time horizon (1970–2014 deforested areas). (b) Net Hg emissions  
 561 reductions from land use policies (this study) are compared to primary anthropogenic emissions  
 562 policies, whose impacts have been quantified in the literature<sup>85–90</sup>. ASGM refers to artisanal and  
 563 small-scale gold mining. For land use scenarios, “Amazon conservation by 2050” refers to the net  
 564 emissions reductions in the 2050 governance (GOV) from the business-as-usual (BAU)  
 565 simulations and “Global reforestation scenario” compares the net emissions reductions in the  
 566 reforestation scenario (RFR) compared to the reference simulation (HIST). Error bars for this  
 567 study refer to the 95% confidence interval based on model parameter uncertainties.

568

## 569 Acknowledgments

570 This work was funded by the Swiss National Science Foundation through an Early  
 571 Postdoc.Mobility grant to A.F. (P2EZP2\_195424) and an Ambizione grant to M.J.  
 572 (PZ00P2\_174101), a grant (#1924148) from the US National Science Foundation to  
 573 N.E.S., and an Academic Transition Grant from Eawag to J.B. We thank Ronny Meier  
 574 and Michael Windisch for assistance in processing the reforestation potential dataset. We  
 575 thank Luiz D. Lacerda for sharing Hg data from Brazil. We acknowledge all researchers  
 576 involved in conducting field studies measuring the impact of deforestation on Hg fluxes.

577 **Code and Data Availability**

578 Model code, analysis scripts, and simulation data supporting the results of this study are  
579 published in Zenodo (<https://doi.org/10.5281/zenodo.8364698>) under a CC BY 4.0  
580 license (<https://creativecommons.org/licenses/by/4.0/>).

581 **Associated Content**

583 **Supporting Information.** Further supporting information can be found in the following  
584 files:

585 Soil emissions parametrization; Observations of deforestation fluxes; Global  
586 deforestation-driven emissions estimates; Parameters for uncertainty analysis;  
587 Scenario maps; Erosion calculations; Atmospheric concentration impacts (PDF)

588

589 Tabulated dataset of literature Hg deforestation flux measurements (XLSX)

590

591 **Author Contributions**

592 All authors conceived the study. M.J., J.B., and A.F. compiled Hg field data through  
593 literature review. A.F. and P.B performed the simulations. All authors contributed to the  
594 data analysis. A.F. wrote the draft of the paper with contributions and revisions from all  
595 authors.

596

597 **References**

- 598 (1) Sheehan, M. C.; Burke, T. A.; Navas-Acien, A.; Breysse, P. N.; McGready, J.; Fox, M. A.  
599 Global Methylmercury Exposure from Seafood Consumption and Risk of Developmental  
600 Neurotoxicity: A Systematic Review. *Bull. World Health Organ.* **2014**, *92* (4), 254-269F.  
601 <https://doi.org/10.2471/BLT.12.116152>.
- 602 (2) Zhang, Y.; Song, Z.; Huang, S.; Zhang, P.; Peng, Y.; Wu, P.; Gu, J.; Dutkiewicz, S.; Zhang,  
603 H.; Wu, S.; Wang, F.; Chen, L.; Wang, S.; Li, P. Global Health Effects of Future  
604 Atmospheric Mercury Emissions. *Nat Commun* **2021**, *12* (1), 3035.  
605 <https://doi.org/10.1038/s41467-021-23391-7>.
- 606 (3) Bellanger, M.; Pichery, C.; Aerts, D.; Berglund, M.; Castaño, A.; Čejchanová, M.; Crettaz,  
607 P.; Davidson, F.; Esteban, M.; Fischer, M. E.; Gurzau, A. E.; Halzlova, K.; Katsonouri, A.;  
608 Knudsen, L. E.; Kolossa-Gehring, M.; Koppen, G.; Ligocka, D.; Miklavčič, A.; Reis, M. F.;  
609 Rudnai, P.; Tratnik, J. S.; Weihe, P.; Budtz-Jørgensen, E.; Grandjean, P.; DEMO/COPHES.  
610 Economic Benefits of Methylmercury Exposure Control in Europe: Monetary Value of  
611 Neurotoxicity Prevention. *Environ Health* **2013**, *12* (1), 3. <https://doi.org/10.1186/1476-069X-12-3>.

613 (4) Outridge, P. M.; Mason, R. P.; Wang, F.; Guerrero, S.; Heimbürger-Boavida, L. E. Updated  
614 Global and Oceanic Mercury Budgets for the United Nations Global Mercury Assessment  
615 2018. *Environ. Sci. Technol.* **2018**, acs.est.8b01246.  
616 <https://doi.org/10.1021/acs.est.8b01246>.

617 (5) Shah, V.; Jacob, D. J.; Thackray, C. P.; Wang, X.; Sunderland, E. M.; Dibble, T. S.; Saiz-  
618 Lopez, A.; Černušák, I.; Kellö, V.; Castro, P. J.; Wu, R.; Wang, C. Improved Mechanistic  
619 Model of the Atmospheric Redox Chemistry of Mercury. *Environ. Sci. Technol.* **2021**, 55  
620 (21), 14445–14456. <https://doi.org/10.1021/acs.est.1c03160>.

621 (6) UNTC. *Minamata Convention on Mercury*; 2013.  
622 [https://treaties.un.org/Pages/ViewDetails.aspx?src=TREATY&mtdsg\\_no=XXVII-17&chapter=27](https://treaties.un.org/Pages/ViewDetails.aspx?src=TREATY&mtdsg_no=XXVII-17&chapter=27).

624 (7) Amos, H. M.; Jacob, D. J.; Streets, D. G.; Sunderland, E. M. Legacy Impacts of All-Time  
625 Anthropogenic Emissions on the Global Mercury Cycle. *Global Biogeochem. Cycles* **2013**,  
626 27 (2), 410–421. <https://doi.org/10.1002/gbc.20040>.

627 (8) Zhou, J.; Obrist, D.; Dastoor, A.; Jiskra, M.; Ryjkov, A. Vegetation Uptake of Mercury and  
628 Impacts on Global Cycling. *Nat. Rev. Earth Environ.* **2021**, 2 (4), 269–284.  
629 <https://doi.org/10.1038/s43017-021-00146-y>.

630 (9) UNEP. *Global Mercury Assessment 2018*; UN Environment Programme, Chemicals and  
631 Health Branch. Geneva, Switzerland, 2019.

632 (10) Schaefer, K.; Elshorbany, Y.; Jafarov, E.; Schuster, P. F.; Striegl, R. G.; Wickland, K. P.;  
633 Sunderland, E. M. Potential Impacts of Mercury Released from Thawing Permafrost. *Nat. Commun.* **2020**, 11 (1), 4650. <https://doi.org/10.1038/s41467-020-18398-5>.

635 (11) Smith-Downey, N. V.; Sunderland, E. M.; Jacob, D. J. Anthropogenic Impacts on Global  
636 Storage and Emissions of Mercury from Terrestrial Soils: Insights from a New Global  
637 Model. *J. Geophys. Res.* **2010**, 115 (G3), G03008. <https://doi.org/10.1029/2009JG001124>.

638 (12) Jiskra, M.; Sonke, J. E.; Obrist, D.; Bieser, J.; Ebinghaus, R.; Myhre, C. L.; Pfaffhuber, K.  
639 A.; Wängberg, I.; Kyllönen, K.; Worthy, D.; Martin, L. G.; Labuschagne, C.; Mkololo, T.;  
640 Ramonet, M.; Magand, O.; Dommergue, A. A Vegetation Control on Seasonal Variations in  
641 Global Atmospheric Mercury Concentrations. *Nature Geosci.* **2018**, 11 (4), 244–250.  
642 <https://doi.org/10.1038/s41561-018-0078-8>.

643 (13) Fostier, A. H.; Melendez-Perez, J. J.; Richter, L. Litter Mercury Deposition in the  
644 Amazonian Rainforest. *Environ. Pollut.* **2015**, 206, 605–610.  
645 <https://doi.org/10.1016/j.envpol.2015.08.010>.

646 (14) IPCC. *Climate Change and Land: An IPCC Special Report on Climate Change,  
647 Desertification, Land Degradation, Sustainable Land Management, Food Security, and  
648 Greenhouse Gas Fluxes in Terrestrial Ecosystems*; Shukla, P. R., Skeg, J., Calvo Buendia,  
649 E., Masson-Delmotte, V., Pörtner, H.-O., Roberts, D. C., Zhai, P., Slade, R., Connors, S.,  
650 van Diemen, S., Ferrat, M., Haughey, E., Luz, S., Pathak, M., Petzold, J., Portugal Pereira,  
651 J., Vyas, P., Huntley, E., Kissick, K., Belkacemi, M., Malley, J., Eds.; 2019.

652 (15) Zhang, H.; Holmes, C. D.; Wu, S. Impacts of Changes in Climate, Land Use and Land  
653 Cover on Atmospheric Mercury. *Atmos. Environ.* **2016**, 141, 230–244.  
654 <https://doi.org/10.1016/j.atmosenv.2016.06.056>.

655 (16) UNFCCC. *The Paris Agreement*; 2015. <https://unfccc.int/process-and-meetings/the-paris-agreement/the-paris-agreement>.

657 (17) Adler Miserendino, R.; Guimarães, J. R. D.; Schudel, G.; Ghosh, S.; Godoy, J. M.;  
658 Silbergeld, E. K.; Lees, P. S. J.; Bergquist, B. A. Mercury Pollution in Amapá, Brazil:  
659 Mercury Amalgamation in Artisanal and Small-Scale Gold Mining or Land-Cover and  
660 Land-Use Changes? *ACS Earth Space Chem.* **2018**, 2 (5), 441–450.  
661 <https://doi.org/10.1021/acsearthspacechem.7b00089>.

662 (18) Carpi, A.; Fostier, A. H.; Orta, O. R.; dos Santos, J. C.; Gittings, M. Gaseous Mercury  
663 Emissions from Soil Following Forest Loss and Land Use Changes: Field Experiments in  
664 the United States and Brazil. *Atmos. Environ.* **2014**, *96*, 423–429.  
665 <https://doi.org/10.1016/j.atmosenv.2014.08.004>.

666 (19) Melendez-Perez, J. J.; Fostier, A. H.; Carvalho, J. A.; Windmöller, C. C.; Santos, J. C.;  
667 Carpi, A. Soil and Biomass Mercury Emissions during a Prescribed Fire in the Amazonian  
668 Rain Forest. *Atmospheric Environment* **2014**, *96*, 415–422.  
669 <https://doi.org/10.1016/j.atmosenv.2014.06.032>.

670 (20) Roulet, M.; Lucotte, M.; Farella, N.; Serique, G.; Coelho, H.; Passos, S.; Mergler, D.  
671 Effects of Recent Human Colonization on the Presence of Mercury in Amazonian  
672 Ecosystems. *Water Air Soil Pollut.* **1999**, *112*, 297–313.

673 (21) Fostier, A. H.; Forti, M. C.; Guimarães, J. R.; Melfi, A. J.; Boulet, R.; Espirito Santo, C. M.;  
674 Krug, F. J. Mercury Fluxes in a Natural Forested Amazonian Catchment (Serra Do Navio,  
675 Amapá State, Brazil). *Sci. Total Environ.* **2000**, *260* (1–3), 201–211.  
676 [https://doi.org/10.1016/S0048-9697\(00\)00564-7](https://doi.org/10.1016/S0048-9697(00)00564-7).

677 (22) Obermeier, W. A.; Nabel, J. E. M. S.; Loughran, T.; Hartung, K.; Bastos, A.; Havermann,  
678 F.; Anthoni, P.; Arneth, A.; Goll, D. S.; Lienert, S.; Lombardozzi, D.; Luyssaert, S.;  
679 McGuire, P. C.; Melton, J. R.; Poulter, B.; Sitch, S.; Sullivan, M. O.; Tian, H.; Walker, A.  
680 P.; Wiltshire, A. J.; Zaehle, S.; Pongratz, J. Modelled Land Use and Land Cover Change  
681 Emissions – a Spatio-Temporal Comparison of Different Approaches. *Earth Syst. Dynam.*  
682 **2021**, *12* (2), 635–670. <https://doi.org/10.5194/esd-12-635-2021>.

683 (23) Feinberg, A.; Dlamini, T.; Jiskra, M.; Shah, V.; Selin, N. E. Evaluating Atmospheric  
684 Mercury (Hg) Uptake by Vegetation in a Chemistry-Transport Model. *Environ. Sci.:  
685 Processes Impacts* **2022**, *24* (9), 1303–1318. <https://doi.org/10.1039/D2EM00032F>.

686 (24) Wang, X.; Lin, C.-J.; Yuan, W.; Sommar, J.; Zhu, W.; Feng, X. Emission-Dominated Gas  
687 Exchange of Elemental Mercury Vapor over Natural Surfaces in China. *Atmos. Chem. Phys.*  
688 **2016**, *16* (17), 11125–11143. <https://doi.org/10.5194/acp-16-11125-2016>.

689 (25) Gatti, L. V.; Basso, L. S.; Miller, J. B.; Gloor, M.; Gatti Domingues, L.; Cassol, H. L. G.;  
690 Tejada, G.; Aragão, L. E. O. C.; Nobre, C.; Peters, W.; Marani, L.; Arai, E.; Sanches, A. H.;  
691 Corrêa, S. M.; Anderson, L.; Von Randow, C.; Correia, C. S. C.; Crispim, S. P.; Neves, R.  
692 A. L. Amazonia as a Carbon Source Linked to Deforestation and Climate Change. *Nature*  
693 **2021**, *595* (7867), 388–393. <https://doi.org/10.1038/s41586-021-03629-6>.

694 (26) Tyukavina, A.; Hansen, M. C.; Potapov, P. V.; Stehman, S. V.; Smith-Rodriguez, K.; Okpa,  
695 C.; Aguilar, R. Types and Rates of Forest Disturbance in Brazilian Legal Amazon, 2000–  
696 2013. *Sci. Adv.* **2017**, *3* (4), e1601047. <https://doi.org/10.1126/sciadv.1601047>.

697 (27) Soares-Filho, B. S.; Nepstad, D. C.; Curran, L. M.; Cerqueira, G. C.; Garcia, R. A.; Ramos,  
698 C. A.; Voll, E.; McDonald, A.; Lefebvre, P.; Schlesinger, P. Modelling Conservation in the  
699 Amazon Basin. *Nature* **2006**, *440* (7083), 520–523. <https://doi.org/10.1038/nature04389>.

700 (28) IPCC. Summary for Policymakers. In *Climate Change 2022: Mitigation of Climate Change.*  
701 *Contribution of Working Group III to the Sixth Assessment Report of the Intergovernmental  
702 Panel on Climate Change*; [P.R. Shukla, J. Skea, R. Slade, A. Al Khourdajie, R. van  
703 Diemen, D. McCollum, M. Pathak, S. Some, P. Vyas, R. Fradera, M. Belkacemi, A. Hasija,  
704 G. Lisboa, S. Luz, J. Malley, (eds.)]. Cambridge University Press, Cambridge, UK and New  
705 York, NY, USA.

706 (29) Holl, K. D.; Brancalion, P. H. S. Tree Planting Is Not a Simple Solution. *Science* **2020**, *368*  
707 (6491), 580–581. <https://doi.org/10.1126/science.aba8232>.

708 (30) Griscom, B. W.; Adams, J.; Ellis, P. W.; Houghton, R. A.; Lomax, G.; Miteva, D. A.;  
709 Schlesinger, W. H.; Shoch, D.; Siikamäki, J. V.; Smith, P.; Woodbury, P.; Zganjar, C.;  
710 Blackman, A.; Campari, J.; Conant, R. T.; Delgado, C.; Elias, P.; Gopalakrishna, T.;  
711 Hamsik, M. R.; Herrero, M.; Kiesecker, J.; Landis, E.; Laestadius, L.; Leavitt, S. M.;

712 Minnemeyer, S.; Polasky, S.; Potapov, P.; Putz, F. E.; Sanderman, J.; Silvius, M.;  
713 Wollenberg, E.; Fargione, J. Natural Climate Solutions. *Proc. Natl. Acad. Sci. U.S.A.* **2017**,  
714 *114* (44), 11645–11650. <https://doi.org/10.1073/pnas.1710465114>.

715 (31) Gelaro, R.; McCarty, W.; Suárez, M. J.; Todling, R.; Molod, A.; Takacs, L.; Randles, C. A.;  
716 Darmenov, A.; Bosilovich, M. G.; Reichle, R.; Wargan, K.; Coy, L.; Cullather, R.; Draper,  
717 C.; Akella, S.; Buchard, V.; Conaty, A.; Silva, A. M. da; Gu, W.; Kim, G.-K.; Koster, R.;  
718 Lucchesi, R.; Merkova, D.; Nielsen, J. E.; Partyka, G.; Pawson, S.; Putman, W.; Rienecker,  
719 M.; Schubert, S. D.; Sienkiewicz, M.; Zhao, B. The Modern-Era Retrospective Analysis for  
720 Research and Applications, Version 2 (MERRA-2). *J. Clim.* **2017**, *30* (14), 5419–5454.  
721 <https://doi.org/10.1175/JCLI-D-16-0758.1>.

722 (32) Horowitz, H. M.; Jacob, D. J.; Zhang, Y.; Dibble, T. S.; Slemr, F.; Amos, H. M.; Schmidt,  
723 J. A.; Corbitt, E. S.; Marais, E. A.; Sunderland, E. M. A New Mechanism for Atmospheric  
724 Mercury Redox Chemistry: Implications for the Global Mercury Budget. *Atmos. Chem.  
725 Phys.* **2017**, *17* (10), 6353–6371. <https://doi.org/10.5194/acp-17-6353-2017>.

726 (33) Amos, H. M.; Jacob, D. J.; Holmes, C. D.; Fisher, J. A.; Wang, Q.; Yantosca, R. M.;  
727 Corbitt, E. S.; Galarneau, E.; Rutter, A. P.; Gustin, M. S.; Steffen, A.; Schauer, J. J.;  
728 Graydon, J. A.; Louis, V. L. St.; Talbot, R. W.; Edgerton, E. S.; Zhang, Y.; Sunderland, E.  
729 M. Gas-Particle Partitioning of Atmospheric Hg(II) and Its Effect on Global Mercury  
730 Deposition. *Atmos. Chem. Phys.* **2012**, *12* (1), 591–603. <https://doi.org/10.5194/acp-12-591-2012>.

732 (34) Wang, Y.; Jacob, D. J.; Logan, J. A. Global Simulation of Tropospheric O<sub>3</sub>-NO<sub>x</sub>-  
733 Hydrocarbon Chemistry: 1. Model Formulation. *J. Geophys. Res.* **1998**, *103* (D9), 10713–  
734 10725. <https://doi.org/10.1029/98JD00158>.

735 (35) Fisher, J. A.; Jacob, D. J.; Wang, Q.; Bahreini, R.; Carouge, C. C.; Cubison, M. J.; Dibb, J.  
736 E.; Diehl, T.; Jimenez, J. L.; Leibensperger, E. M.; Lu, Z.; Meinders, M. B. J.; Pye, H. O.  
737 T.; Quinn, P. K.; Sharma, S.; Streets, D. G.; van Donkelaar, A.; Yantosca, R. M. Sources,  
738 Distribution, and Acidity of Sulfate–Ammonium Aerosol in the Arctic in Winter–Spring.  
739 *Atmos. Environ.* **2011**, *45* (39), 7301–7318. <https://doi.org/10.1016/j.atmosenv.2011.08.030>.

740 (36) Gibbs, H. K. Olson's Major World Ecosystem Complexes Ranked by Carbon in Live  
741 Vegetation: An Updated Database Using the GLC2000 Land Cover Product (NDP-017b).  
742 <https://www.osti.gov/biblio/1389498>, 2006. **2006**.

743 (37) Yuan, H.; Dai, Y.; Xiao, Z.; Ji, D.; Shangguan, W. Reprocessing the MODIS Leaf Area  
744 Index Products for Land Surface and Climate Modelling. *Remote Sens. Environ.* **2011**, *115*  
745 (5), 1171–1187. <https://doi.org/10.1016/j.rse.2011.01.001>.

746 (38) Steenhuisen, F.; Wilson, S. J. Development and Application of an Updated Geospatial  
747 Distribution Model for Gridding 2015 Global Mercury Emissions. *Atmos. Environ.* **2019**,  
748 *211*, 138–150. <https://doi.org/10.1016/j.atmosenv.2019.05.003>.

749 (39) van der Werf, G. R.; Randerson, J. T.; Giglio, L.; van Leeuwen, T. T.; Chen, Y.; Rogers, B.  
750 M.; Mu, M.; van Marle, M. J. E.; Morton, D. C.; Collatz, G. J.; Yokelson, R. J.; Kasibhatla,  
751 P. S. Global Fire Emissions Estimates during 1997–2016. *Earth Syst. Sci. Data* **2017**, *9* (2),  
752 697–720. <https://doi.org/10.5194/essd-9-697-2017>.

753 (40) Strode, S. A.; Jaeglé, L.; Selin, N. E.; Jacob, D. J.; Park, R. J.; Yantosca, R. M.; Mason, R.  
754 P.; Slemr, F. Air-Sea Exchange in the Global Mercury Cycle. *Global Biogeochem. Cycles*  
755 **2007**, *21* (1), GB1017. <https://doi.org/10.1029/2006GB002766>.

756 (41) Khan, T. R.; Obrist, D.; Agnan, Y.; Selin, N. E.; Perlinger, J. A. Atmosphere-Terrestrial  
757 Exchange of Gaseous Elemental Mercury: Parameterization Improvement through Direct  
758 Comparison with Measured Ecosystem Fluxes. *Environ. Sci.: Processes Impacts* **2019**, *21*  
759 (10), 1699–1712. <https://doi.org/10.1039/C9EM00341J>.

760 (42) Selin, N. E.; Jacob, D. J.; Yantosca, R. M.; Strode, S.; Jaeglé, L.; Sunderland, E. M. Global  
761 3-D Land-Ocean-Atmosphere Model for Mercury: Present-Day versus Preindustrial Cycles

762 and Anthropogenic Enrichment Factors for Deposition. *Global Biogeochem. Cycles* **2008**,  
 763 22 (2), GB2011. <https://doi.org/10.1029/2007GB003040>.

764 (43) Verstraete, M. M. Radiation Transfer in Plant Canopies: Transmission of Direct Solar  
 765 Radiation and the Role of Leaf Orientation. *J. Geophys. Res.* **1987**, 92 (D9), 10985.  
 766 <https://doi.org/10.1029/JD092iD09p10985>.

767 (44) Dinerstein, E.; Olson, D.; Joshi, A.; Vynne, C.; Burgess, N. D.; Wikramanayake, E.; Hahn,  
 768 N.; Palminteri, S.; Hedao, P.; Noss, R.; Hansen, M.; Locke, H.; Ellis, E. C.; Jones, B.;  
 769 Barber, C. V.; Hayes, R.; Kormos, C.; Martin, V.; Crist, E.; Sechrest, W.; Price, L.; Baillie,  
 770 J. E. M.; Weeden, D.; Suckling, K.; Davis, C.; Sizer, N.; Moore, R.; Thau, D.; Birch, T.;  
 771 Potapov, P.; Turubanova, S.; Tyukavina, A.; de Souza, N.; Pintea, L.; Brito, J. C.;  
 772 Llewellyn, O. A.; Miller, A. G.; Patzelt, A.; Ghazanfar, S. A.; Timberlake, J.; Klöser, H.;  
 773 Shennan-Farpón, Y.; Kindt, R.; Lillesø, J.-P. B.; van Breugel, P.; Graudal, L.; Voge, M.;  
 774 Al-Shammari, K. F.; Saleem, M. An Ecoregion-Based Approach to Protecting Half the  
 775 Terrestrial Realm. *BioScience* **2017**, 67 (6), 534–545. <https://doi.org/10.1093/biosci/bix014>.

776 (45) Hurtt, G. C.; Chini, L.; Sahajpal, R.; Frolking, S.; Bodirsky, B. L.; Calvin, K.; Doelman, J.  
 777 C.; Fisk, J.; Fujimori, S.; Klein Goldewijk, K.; Hasegawa, T.; Havlik, P.; Heinimann, A.;  
 778 Humpenöder, F.; Jungclaus, J.; Kaplan, J. O.; Kennedy, J.; Krisztin, T.; Lawrence, D.;  
 779 Lawrence, P.; Ma, L.; Mertz, O.; Ponrath, J.; Popp, A.; Poulter, B.; Riahi, K.; Shevliakova,  
 780 E.; Stehfest, E.; Thornton, P.; Tubiello, F. N.; van Vuuren, D. P.; Zhang, X. Harmonization  
 781 of Global Land Use Change and Management for the Period 850–2100 (LUH2) for CMIP6.  
 782 *Geosci. Model Dev.* **2020**, 13 (11), 5425–5464. <https://doi.org/10.5194/gmd-13-5425-2020>.

783 (46) Hosonuma, N.; Herold, M.; De Sy, V.; De Fries, R. S.; Brockhaus, M.; Verchot, L.;  
 784 Angelsen, A.; Romijn, E. An Assessment of Deforestation and Forest Degradation Drivers  
 785 in Developing Countries. *Environ. Res. Lett.* **2012**, 7 (4), 044009.  
 786 <https://doi.org/10.1088/1748-9326/7/4/044009>.

787 (47) Geist, H. J.; Lambin, E. F. Proximate Causes and Underlying Driving Forces of Tropical  
 788 Deforestation. *BioScience* **2002**, 52 (2), 143. [https://doi.org/10.1641/0006-3568\(2002\)052\[0143:PCAUDF\]2.0.CO;2](https://doi.org/10.1641/0006-3568(2002)052[0143:PCAUDF]2.0.CO;2).

789 (48) Gerson, J. R.; Szponar, N.; Zambrano, A. A.; Bergquist, B.; Broadbent, E.; Driscoll, C. T.;  
 790 Erkenswick, G.; Evers, D. C.; Fernandez, L. E.; Hsu-Kim, H.; Inga, G.; Lansdale, K. N.;  
 791 Marchese, M. J.; Martinez, A.; Moore, C.; Pan, W. K.; Purizaca, R. P.; Sánchez, V.; Silman,  
 792 M.; Ury, E. A.; Vega, C.; Watsa, M.; Bernhardt, E. S. Amazon Forests Capture High Levels  
 793 of Atmospheric Mercury Pollution from Artisanal Gold Mining. *Nat Commun* **2022**, 13 (1),  
 794 559. <https://doi.org/10.1038/s41467-022-27997-3>.

795 (49) Almeida, M. D.; Lacerda, L. D.; Bastos, W. R.; Herrmann, J. C. Mercury Loss from Soils  
 796 Following Conversion from Forest to Pasture in Rondônia, Western Amazon, Brazil.  
 797 *Environmental Pollution* **2005**, 137 (2), 179–186.  
 798 <https://doi.org/10.1016/j.envpol.2005.02.026>.

799 (50) Almeida, M. D.; Marins, R. V.; Paraquetti, H. H. M.; Bastos, W. R.; Lacerda, L. D.  
 800 Mercury Degassing from Forested and Open Field Soils in Rondônia, Western Amazon,  
 801 Brazil. *Chemosphere* **2009**, 77 (1), 60–66.  
 802 <https://doi.org/10.1016/j.chemosphere.2009.05.018>.

803 (51) Lacerda, L. D.; de Souza, M.; Ribeiro, M. G. The Effects of Land Use Change on Mercury  
 804 Distribution in Soils of Alta Floresta, Southern Amazon. *Environmental Pollution* **2004**,  
 805 129 (2), 247–255. <https://doi.org/10.1016/j.envpol.2003.10.013>.

806 (52) Bélieau, A.; Lucotte, M.; Davidson, R.; do Canto Lopes, L. O.; Paquet, S. Early Hg  
 807 Mobility in Cultivated Tropical Soils One Year after Slash-and-Burn of the Primary Forest,  
 808 in the Brazilian Amazon. *Science of The Total Environment* **2009**, 407 (15), 4480–4489.  
 809 <https://doi.org/10.1016/j.scitotenv.2009.04.012>.

811 (53) Bélieau, A.; Lucotte, M.; Davidson, R.; Paquet, S.; Mertens, F.; Passos, C. J.; Romana, C.  
812 A. Reduction of Soil Erosion and Mercury Losses in Agroforestry Systems Compared to  
813 Forests and Cultivated Fields in the Brazilian Amazon. *Journal of Environmental*  
814 *Management* **2017**, *203*, 522–532. <https://doi.org/10.1016/j.jenvman.2017.07.037>.

815 (54) Patry, C.; Davidson, R.; Lucotte, M.; Bélieau, A. Impact of Forested Fallows on Fertility  
816 and Mercury Content in Soils of the Tapajós River Region, Brazilian Amazon. *Science of*  
817 *The Total Environment* **2013**, *458–460*, 228–237.  
818 <https://doi.org/10.1016/j.scitotenv.2013.04.037>.

819 (55) Comte, I.; Lucotte, M.; Davidson, R.; Reis de Carvalho, C. J.; de Assis Oliveira, F.;  
820 Rousseau, G. X. Impacts of Land Uses on Mercury Retention in Long-Time Cultivated  
821 Soils, Brazilian Amazon. *Water Air Soil Pollut* **2013**, *224* (4), 1515.  
822 <https://doi.org/10.1007/s11270-013-1515-3>.

823 (56) Magarelli, G.; Fostier, A. Influence of Deforestation on the Mercury Air/Soil Exchange in  
824 the Negro River Basin, Amazon. *Atmos. Environ.* **2005**, *39* (39), 7518–7528.  
825 <https://doi.org/10.1016/j.atmosenv.2005.07.067>.

826 (57) Mainville, N.; Webb, J.; Lucotte, M.; Davidson, R.; Betancourt, O.; Cueva, E.; Mergler, D.  
827 Decrease of Soil Fertility and Release of Mercury Following Deforestation in the Andean  
828 Amazon, Napo River Valley, Ecuador. *Science of The Total Environment* **2006**, *368* (1),  
829 88–98. <https://doi.org/10.1016/j.scitotenv.2005.09.064>.

830 (58) Roulet, M.; Lucotte, M.; Saint-Aubin, A.; Tran, S.; Rhéault, I.; Farella, N.; De Jesus Da  
831 silva, E.; Dezencourt, J.; Sousa Passos, C.-J.; Santos Soares, G.; Guimarães, J.-R. D.;  
832 Mergler, D.; Amorim, M. The Geochemistry of Mercury in Central Amazonian Soils  
833 Developed on the Alter-Do-Chão Formation of the Lower Tapajós River Valley, Pará State,  
834 Brazil. *Science of The Total Environment* **1998**, *223* (1), 1–24.  
835 [https://doi.org/10.1016/S0048-9697\(98\)00265-4](https://doi.org/10.1016/S0048-9697(98)00265-4).

836 (59) Wasserman, J. C.; Campos, R. C.; Hacon, S. de S.; Farias, R. A.; Caires, S. M. Mercury in  
837 Soils and Sediments from Gold Mining Liabilities in Southern Amazonia. *Quím. Nova*  
838 **2007**, *30* (4). <https://doi.org/10.1590/S0100-40422007000400003>.

839 (60) Homann, P. S.; Darbyshire, R. L.; Bormann, B. T.; Morrisette, B. A. Forest Structure  
840 Affects Soil Mercury Losses in the Presence and Absence of Wildfire. *Environ. Sci.*  
841 *Technol.* **2015**, *49* (21), 12714–12722. <https://doi.org/10.1021/acs.est.5b03355>.

842 (61) Gamby, R. L.; Hammerschmidt, C. R.; Costello, D. M.; Lamborg, C. H.; Runkle, J. R.  
843 Deforestation and Cultivation Mobilize Mercury from Topsoil. *Science of The Total*  
844 *Environment* **2015**, *532*, 467–473. <https://doi.org/10.1016/j.scitotenv.2015.06.025>.

845 (62) Mazur, M.; Mitchell, C. P. J.; Eckley, C. S.; Eggert, S. L.; Kolka, R. K.; Sebestyen, S. D.;  
846 Swain, E. B. Gaseous Mercury Fluxes from Forest Soils in Response to Forest Harvesting  
847 Intensity: A Field Manipulation Experiment. *Science of The Total Environment* **2014**, *496*,  
848 678–687. <https://doi.org/10.1016/j.scitotenv.2014.06.058>.

849 (63) Ma, M.; Wang, D.; Sun, R.; Shen, Y.; Huang, L. Gaseous Mercury Emissions from  
850 Subtropical Forested and Open Field Soils in a National Nature Reserve, Southwest China.  
851 *Atmospheric Environment* **2013**, *64*, 116–123.  
852 <https://doi.org/10.1016/j.atmosenv.2012.09.038>.

853 (64) Eckley, C. S.; Eagles-Smith, C.; Tate, M. T.; Krabbenhoft, D. P. Surface-Air Mercury  
854 Fluxes and a Watershed Mass Balance in Forested and Harvested Catchments.  
855 *Environmental Pollution* **2021**, *277*, 116869. <https://doi.org/10.1016/j.envpol.2021.116869>.

856 (65) Ramankutty, N.; Gibbs, H. K.; Achard, F.; Defries, R.; Foley, J. A.; Houghton, R. A.  
857 Challenges to Estimating Carbon Emissions from Tropical Deforestation. *Global Change*  
858 *Biol* **2007**, *13* (1), 51–66. <https://doi.org/10.1111/j.1365-2486.2006.01272.x>.

859 (66) Crespo-Lopez, M. E.; Augusto-Oliveira, M.; Lopes-Araujo, A.; Santos-Sacramento, L.;  
860 Yuki Takeda, P.; Macchi, B. de M.; do Nascimento, J. L. M.; Maia, C. S. F.; Lima, R. R.;

861 Arrifano, G. P. Mercury: What Can We Learn from the Amazon? *Environment*  
 862 *International* **2021**, *146*, 106223. <https://doi.org/10.1016/j.envint.2020.106223>.

863 (67) Michelazzo, P. A. M.; Fostier, A. H.; Magarelli, G.; Santos, J. C.; de Carvalho, J. A.  
 864 Mercury Emissions from Forest Burning in Southern Amazon. *Geophys. Res. Lett.* **2010**, *37*  
 865 (9), L09809. <https://doi.org/10.1029/2009GL042220>.

866 (68) Lovejoy, T. E.; Nobre, C. Amazon Tipping Point. *Sci. Adv.* **2018**, *4* (2), eaat2340.

867 (69) Alves de Oliveira, B. F.; Bottino, M. J.; Nobre, P.; Nobre, C. A. Deforestation and Climate  
 868 Change Are Projected to Increase Heat Stress Risk in the Brazilian Amazon. *Commun. Earth Environ.* **2021**, *2* (1), 207. <https://doi.org/10.1038/s43247-021-00275-8>.

869 (70) Griscom, B. W.; Adams, J.; Ellis, P. W.; Houghton, R. A.; Lomax, G.; Miteva, D. A.;  
 870 Schlesinger, W. H.; Shoch, D.; Siikamäki, J. V.; Smith, P.; Woodbury, P.; Zganjar, C.;  
 871 Blackman, A.; Campari, J.; Conant, R. T.; Delgado, C.; Elias, P.; Gopalakrishna, T.;  
 872 Hamsik, M. R.; Herrero, M.; Kiesecker, J.; Landis, E.; Laestadius, L.; Leavitt, S. M.;  
 873 Minnemeyer, S.; Polasky, S.; Potapov, P.; Putz, F. E.; Sanderman, J.; Silvius, M.;  
 874 Wollenberg, E.; Fargione, J. *Global Reforestation Potential Map*; Zenodo, 2017.  
 875 <https://doi.org/10.5281/zenodo.883444>.

876 (71) McKay, M. D.; Beckman, R. J.; Conover, W. J. Comparison of Three Methods for Selecting  
 877 Values of Input Variables in the Analysis of Output from a Computer Code. *Technometrics*  
 878 **1979**, *21* (2), 239–245. <https://doi.org/10.1080/00401706.1979.10489755>.

879 (72) Pacyna, J. M.; Travnikov, O.; De Simone, F.; Hedgecock, I. M.; Sundseth, K.; Pacyna, E.  
 880 G.; Steenhuisen, F.; Pirrone, N.; Munthe, J.; Kindbom, K. Current and Future Levels of  
 881 Mercury Atmospheric Pollution on a Global Scale. *Atmos. Chem. Phys.* **2016**, *16* (19),  
 882 12495–12511. <https://doi.org/10.5194/acp-16-12495-2016>.

883 (73) Fisher, J. A.; Schneider, L.; Fostier, A.-H.; Guerrero, S.; Guimarães, J. R. D.; Labuschagne,  
 884 C.; Leaner, J. J.; Martin, L. G.; Mason, R. P.; Somerset, V.; Walters, C. A Synthesis of  
 885 Mercury Research in the Southern Hemisphere, Part 2: Anthropogenic Perturbations. *Ambio*  
 886 **2023**, *52* (5), 918–937. <https://doi.org/10.1007/s13280-023-01840-5>.

887 (74) Zhang, Y.; Jacob, D. J.; Horowitz, H. M.; Chen, L.; Amos, H. M.; Krabbenhoft, D. P.;  
 888 Slemr, F.; St. Louis, V. L.; Sunderland, E. M. Observed Decrease in Atmospheric Mercury  
 889 Explained by Global Decline in Anthropogenic Emissions. *Proc. Natl. Acad. Sci. U.S.A.*  
 890 **2016**, *113* (3), 526–531. <https://doi.org/10.1073/pnas.1516312113>.

891 (75) Schartup, A. T.; Thackray, C. P.; Qureshi, A.; Dassuncao, C.; Gillespie, K.; Hanke, A.;  
 892 Sunderland, E. M. Climate Change and Overfishing Increase Neurotoxicant in Marine  
 893 Predators. *Nature* **2019**, *572* (7771), 648–650. <https://doi.org/10.1038/s41586-019-1468-9>.

894 (76) Zhang, Y.; Soerensen, A. L.; Schartup, A. T.; Sunderland, E. M. A Global Model for  
 895 Methylmercury Formation and Uptake at the Base of Marine Food Webs. *Global  
 896 Biogeochem. Cycles* **2020**, *34* (2). <https://doi.org/10.1029/2019GB006348>.

897 (77) Roulet, M.; Guimarães, J.R.D; Lucotte, M. Methylmercury Production and Accumulation in  
 898 Sediments and Soils of an Amazonian Floodplain – Effect of Seasonal Inundation. *Water,  
 899 Air, and Soil Pollution* **2001**, *128*, 41–60.

900 (78) Borrelli, P.; Robinson, D. A.; Panagos, P.; Lugato, E.; Yang, J. E.; Alewell, C.; Wuepper,  
 901 D.; Montanarella, L.; Ballabio, C. Land Use and Climate Change Impacts on Global Soil  
 902 Erosion by Water (2015–2070). *Proc. Natl. Acad. Sci. U.S.A.* **2020**, *117* (36), 21994–22001.  
 903 <https://doi.org/10.1073/pnas.2001403117>.

904 (79) Borrelli, P.; Robinson, D. A.; Fleischer, L. R.; Lugato, E.; Ballabio, C.; Alewell, C.;  
 905 Meusburger, K.; Modugno, S.; Schütt, B.; Ferro, V.; Bagarello, V.; Oost, K. V.;  
 906 Montanarella, L.; Panagos, P. An Assessment of the Global Impact of 21st Century Land  
 907 Use Change on Soil Erosion. *Nat Commun* **2017**, *8* (1), 2013.  
 908 <https://doi.org/10.1038/s41467-017-02142-7>.

909

910 (80) Bastin, J.-F.; Finegold, Y.; Garcia, C.; Mollicone, D.; Rezende, M.; Routh, D.; Zohner, C.  
 911 M.; Crowther, T. W. The Global Tree Restoration Potential. *Science* **2019**, *365* (6448), 76–  
 912 79. <https://doi.org/10.1126/science.aax0848>.

913 (81) Briggs, C.; Gustin, M. S. Building upon the Conceptual Model for Soil Mercury Flux:  
 914 Evidence of a Link Between Moisture Evaporation and Hg Evasion. *Water Air Soil Pollut*  
 915 **2013**, *224* (10), 1744. <https://doi.org/10.1007/s11270-013-1744-5>.

916 (82) Osterwalder, S.; Huang, J.-H.; Shetaya, W. H.; Agnan, Y.; Frossard, A.; Frey, B.; Alewell,  
 917 C.; Kretzschmar, R.; Biester, H.; Obrist, D. Mercury Emission from Industrially  
 918 Contaminated Soils in Relation to Chemical, Microbial, and Meteorological Factors.  
 919 *Environmental Pollution* **2019**, *250*, 944–952. <https://doi.org/10.1016/j.envpol.2019.03.093>.

920 (83) Agnan, Y.; Le Dantec, T.; Moore, C. W.; Edwards, G. C.; Obrist, D. New Constraints on  
 921 Terrestrial Surface–Atmosphere Fluxes of Gaseous Elemental Mercury Using a Global  
 922 Database. *Environ. Sci. Technol.* **2016**, *50* (2), 507–524.  
 923 <https://doi.org/10.1021/acs.est.5b04013>.

924 (84) Yuan, T.; Zhang, P.; Song, Z.; Huang, S.; Wang, X.; Zhang, Y. Buffering Effect of Global  
 925 Vegetation on the Air-Land Exchange of Mercury: Insights from a Novel Terrestrial  
 926 Mercury Model Based on CESM2-CLM5. *Environment International* **2023**, *174*, 107904.  
 927 <https://doi.org/10.1016/j.envint.2023.107904>.

928 (85) Liu, K.; Wu, Q.; Wang, L.; Wang, S.; Liu, T.; Ding, D.; Tang, Y.; Li, G.; Tian, H.; Duan,  
 929 L.; Wang, X.; Fu, X.; Feng, X.; Hao, J. Measure-Specific Effectiveness of Air Pollution  
 930 Control on China’s Atmospheric Mercury Concentration and Deposition during 2013–2017.  
 931 *Environ. Sci. Technol.* **2019**, *53* (15), 8938–8946. <https://doi.org/10.1021/acs.est.9b02428>.

932 (86) EPA. *National Emission Standards for Hazardous Air Pollutants: Coal- and Oil-Fired  
 933 Electric Utility Steam Generating Units—Reconsideration of Supplemental Finding and  
 934 Residual Risk and Technology Review*; EPA–HQ–OAR–2018–0794; FRL–9988–93–OAR;  
 935 2019; pp 2670–2704. <https://www.govinfo.gov/content/pkg/FR-2019-02-07/pdf/2019-00936.pdf>.

936 (87) Environment and Climate Change Canada. *Evaluation of the Effectiveness of Risk  
 937 Management Measures for Mercury*; En14-411/2020E-PDF; 2020; pp 1–43.  
 938 [https://www.canada.ca/en/environment-climate-change/services/management-toxic-  
 940 substances/evaluation-effectiveness-risk-management-measures-mercury.html](https://www.canada.ca/en/environment-climate-change/services/management-toxic-<br/>
  939 substances/evaluation-effectiveness-risk-management-measures-mercury.html).

941 (88) Bruno, D. E.; De Simone, F.; Cinnirella, S.; Hedgecock, I. M.; D’Amore, F.; Pirrone, N.  
 942 Reducing Mercury Emission Uncertainty from Artisanal and Small-Scale Gold Mining  
 943 Using Bootstrap Confidence Intervals: An Assessment of Emission Reduction Scenarios.  
 944 *Atmosphere* **2022**, *14* (1), 62. <https://doi.org/10.3390/atmos14010062>.

945 (89) Mulvaney, K. M.; Selin, N. E.; Giang, A.; Muntean, M.; Li, C.-T.; Zhang, D.; Angot, H.;  
 946 Thackray, C. P.; Karplus, V. J. Mercury Benefits of Climate Policy in China: Addressing  
 947 the Paris Agreement and the Minamata Convention Simultaneously. *Environ. Sci. Technol.*  
 948 **2020**, *54* (3), 1326–1335. <https://doi.org/10.1021/acs.est.9b06741>.

949 (90) Rafaj, P.; Cofala, J.; Kuenen, J.; Wyrwa, A.; Zyśk, J. Benefits of European Climate Policies  
 950 for Mercury Air Pollution. *Atmosphere* **2014**, *5* (1), 45–59.  
 951 <https://doi.org/10.3390/atmos5010045>.

952 (91) Wohlgemuth, L.; Rautio, P.; Ahrends, B.; Russ, A.; Vesterdal, L.; Waldner, P.;  
 953 Timmermann, V.; Eickenscheidt, N.; Fürst, A.; Greve, M.; Roskams, P.; Thimonier, A.;  
 954 Nicolas, M.; Kowalska, A.; Ingerslev, M.; Merilä, P.; Benham, S.; Iacoban, C.; Hoch, G.;  
 955 Alewell, C.; Jiskra, M. Physiological and Climate Controls on Foliar Mercury Uptake by  
 956 European Tree Species. *Biogeosciences* **2022**, *19* (5), 1335–1353.  
 957 <https://doi.org/10.5194/bg-19-1335-2022>.

958 (92) COP26. *Glasgow Leaders’ Declaration on Forests and Land Use*; 2021.  
 959 <https://ukcop26.org/glasgow-leaders-declaration-on-forests-and-land-use/>.

1 **Supplementary Information (SI) for**  
2 **Deforestation as an anthropogenic driver of mercury pollution**

3

4 *Aryeh Feinberg<sup>a</sup>\*, Martin Jiskra<sup>b</sup>\*, Pasquale Borrelli<sup>c</sup>, Jagannath Biswakarma<sup>b,d</sup>, and Noelle*  
5 *E. Selin<sup>a,e</sup>*

6 <sup>a</sup> Institute for Data, Systems, and Society, Massachusetts Institute of Technology, Cambridge,  
7 MA 02139, USA

8 <sup>b</sup> Environmental Geosciences, University of Basel, Basel 4056, Switzerland

9 <sup>c</sup> Department of Science, Roma Tre University, Rome 00146, Italy

10 <sup>d</sup> Department of Water Resources and Drinking Water, Eawag, Dübendorf 8600, Switzerland

11 <sup>e</sup> Department of Earth, Atmospheric, and Planetary Sciences, Massachusetts Institute of  
12 Technology, Cambridge, MA 02139, USA

13 \*Correspondence to: arifeinberg@gmail.com (A.F.); martin.jiskra@gmail.com (M.J.)

14

15 Number of pages: 19

16 Number of figures: 11

17 Number of tables: 6

18

19 **Section S1. Soil emissions parameterization**20 We improved the model's parametrization of  $\text{Hg}^0$  soil emissions by adopting a new formulation for the  
21 parametrization, suggested by Khan et al.<sup>1</sup>:

22 
$$E_{\text{soil}} = aC^bR_g^c \quad (\text{Eq. S1})$$

23 where  $E_{\text{soil}}$  are soil emissions ( $\text{ng m}^{-2} \text{h}^{-1}$ ),  $C$  is the concentration of Hg in soils ( $\mu\text{g g}^{-1}$ ),  $R_g$  is the solar  
24 radiation flux at the ground ( $\text{W m}^{-2}$ ), and  $a$ ,  $b$ , and  $c$  are coefficients.25 As in Selin et al.<sup>2</sup>, the solar radiation at the ground ( $R_g$ ) is determined by considering attenuation of the  
26 solar radiation flux ( $R_S$ ) by shading from the overhead canopy, parametrized by the leaf area index  
27 (LAI):

28 
$$R_g = R_S \exp\left(-\frac{\alpha \text{LAI}}{\cos\theta}\right) \quad (\text{Eq. S2})$$

29 where  $\alpha = 0.5$ , assuming extinction from a random angular distribution of leaves<sup>3</sup> and  $\theta$  is the solar  
30 zenith angle.31 We compiled several relevant observational constraints for the parametrization in Tables S1 and S2.  
32 Observational studies from the Amazon region suggest that deforestation has a large impact on soil  
33 emissions due to removal of canopy shading, showing factors of  $1.8\times$ ,  $6.7\times$ , and  $>31\times$  more emissions  
34 in forested compared to deforested land plots (Table S1). Observational studies from other regions  
35 find a similarly high sensitivity of soil emissions to the presence of forest: open fields in China  
36 showed 6–10 times higher Hg emissions than forests<sup>4</sup> and logging in the US flipped the surface-air  
37 Hg<sup>0</sup> flux from net deposition to net emissions ( $-2.2 \mu\text{g m}^{-2} \text{yr}^{-1}$  to  $+5.5 \mu\text{g m}^{-2} \text{yr}^{-1}$ )<sup>5</sup>. For extratropical  
38 grassland soil emissions, we use the compiled median values from Zhu et al.<sup>6</sup> and Agnan et al.<sup>7</sup>39  
40  
41 We conducted a parameter sweep of  $a$ ,  $b$ , and  $c$ , calculating globally-gridded soil emissions using  
42 annual solar radiation data (Fig. S1). Sensitivity simulations showed that the ratio of deforested to  
43 forested soil emissions in the Amazon (median value 6.7) can tune the exponent for the radiation term  
44 ( $c$  in Eq. S1), i.e., the response of emissions to canopy shading. The exponent for the soil  
45 concentration term ( $b$ ) was tuned with the ratio of deforested Amazon soil emissions (Table S1) to  
46 extratropical grassland soil emissions from the Northern Hemisphere from two review studies<sup>6,7</sup>  
47 (overall Amazon to extratropical ratio of 5.3). Lastly, after these coefficients are tuned, the prefactor  $a$   
48 is adjusted so that predicted annual mean emissions match the observed median magnitudes of  
49 Amazon deforested soil emissions ( $23 \mu\text{g m}^{-2} \text{yr}^{-1}$ ) and extratropical grassland emissions ( $4.3 \mu\text{g m}^{-2}$   
50  $\text{yr}^{-1}$ ).  
5152 We recognize the uncertainties in the observed data used to tune this parametrization, and thus we  
53 constructed 100 alternative parametrizations that fit within observed data bounds (Table S5). These  
54 parametrizations were applied in offline uncertainty analyses to assess 95% confidence intervals in the  
55 fluxes driven by deforestation (Section S4).  
56

59 **Table S1.** Literature review of available  $\text{Hg}^0$  soil emission flux measurements from the Amazon  
60 region, differentiated by land cover type.

Reference	Location	Site	Deforested $\text{Hg}^0$ flux ( $\mu\text{g m}^{-2} \text{yr}^{-1}$ )	Forested $\text{Hg}^0$ flux ( $\mu\text{g m}^{-2} \text{yr}^{-1}$ )	Flux ratio (deforest:forest)
Magarelli and Fostier <sup>8</sup>	Negro River Basin, Brazil	#1	$27 \pm 9$	$0.6 \pm 1.5$	
		#2	19	$-1.0 \pm 0.8$	
		#3	$9.8 \pm 0.7$		
		Mean	18	-0.2	$> 31^a$
Almeida et al. <sup>9</sup>	Rondônia, Brazil	#1	$79 \pm 110$	$44 \pm 18$	1.8
Carpi et al. <sup>10</sup>	Acre, Brazil	#1	$19 \pm 2$	$2.9 \pm 0.8$	6.7
		#2	230 <sup>b</sup>		
<b>Median</b>			<b>23</b>	<b>1.8</b>	<b>6.7</b>

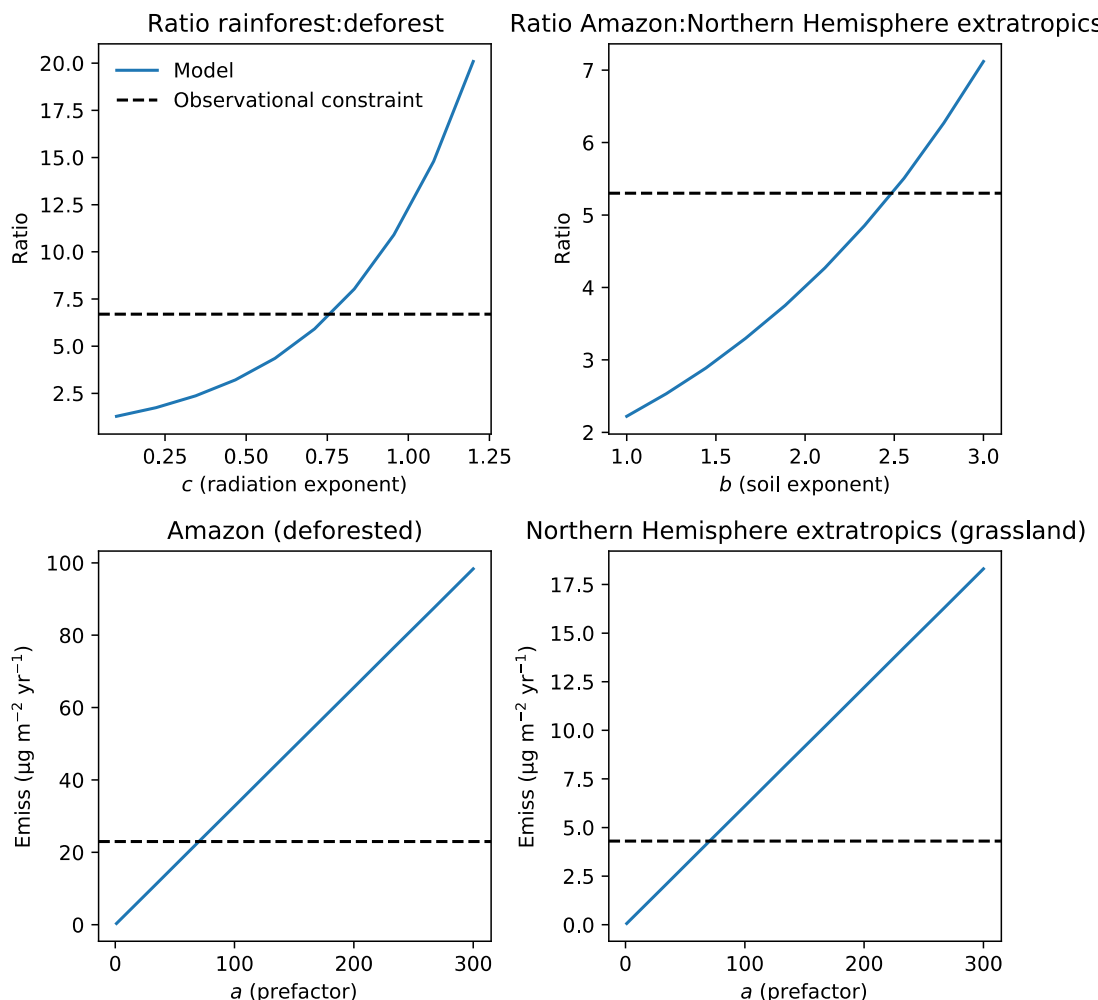
61 <sup>a</sup>lower limit calculated assuming the forested flux is equal to site #1, as site #2 shows negative overall flux;  
62 deforested flux assumed as mean.63 <sup>b</sup>this site was 2-months post-fire and soil temperatures were still elevated; this flux is excluded from ratio  
64 calculations

65

66 **Table S2.** Observational constraints used to tune the soil emissions parametrization.

Constraint	Value	Reference	Coefficient constrained
Amazon deforested soil emissions ( $\mu\text{g m}^{-2} \text{yr}^{-1}$ )	23	Table S1	<i>a</i>
Extratropical grassland soil emissions ( $\mu\text{g m}^{-2} \text{yr}^{-1}$ )	4.3 <sup>†</sup>	Zhu et al. <sup>6</sup> ; Agnan et al. <sup>7</sup>	<i>a</i>
Ratio of Amazon to extratropical soil emissions	5.3	(23:4.3)	<i>b</i>
Ratio of deforested to forested Amazon soil emissions	6.7	Table S1	<i>c</i>

67 <sup>†</sup>average of grassland median  $\text{Hg}^0$  fluxes from the two independent review studies



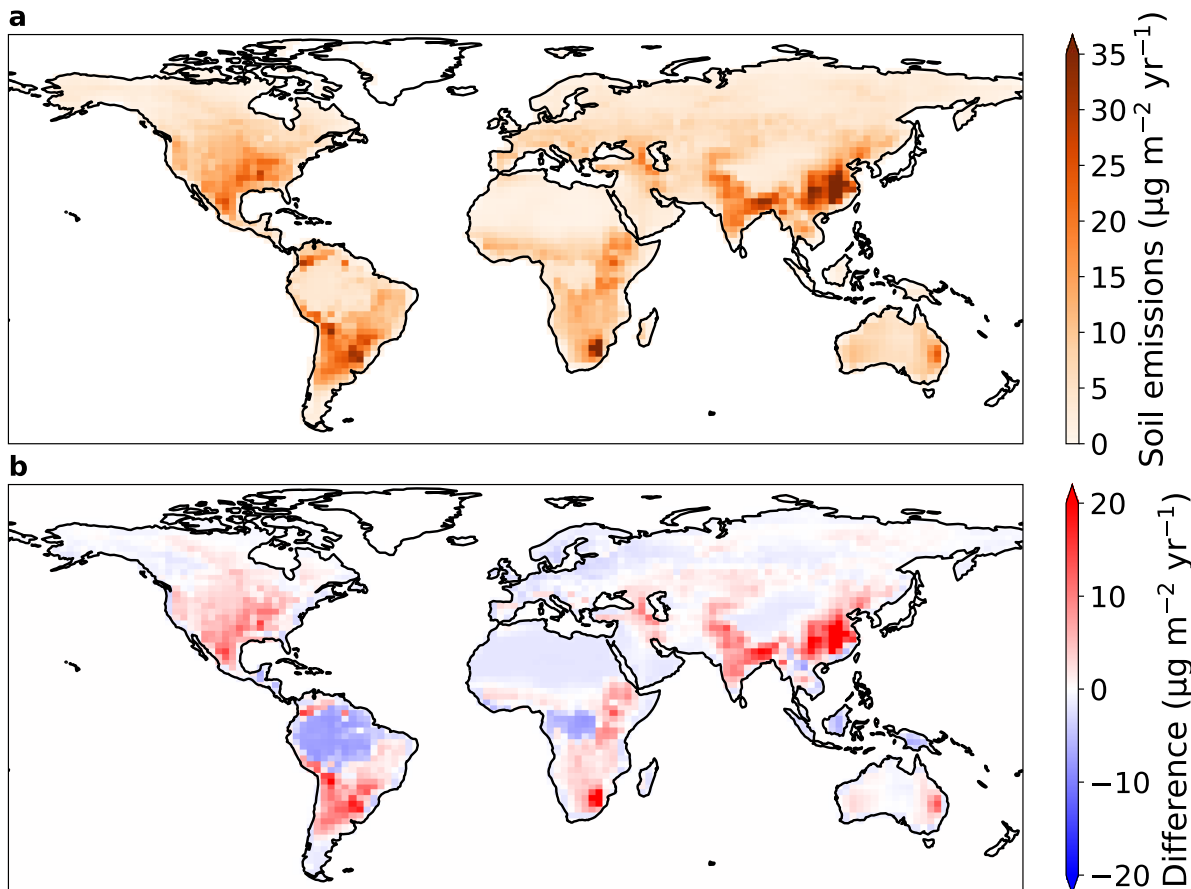
68

69 **Figure S1.** Parameter tuning (Eq. S1) to match observational constraints from Table S2.

70

71 The tuning procedure is illustrated in Fig. S1, yielding best matches for  $a = 71$ ,  $b = 2.5$ , and  
 72  $c = 0.76$ . We compare the gridded annual mean soil emissions from the previous soil emission  
 73 parametrization (GEOS-Chem v12.8) and the current study (Eq. S1) in Fig. S2. Global annual mean  
 74 soil  $\text{Hg}^0$  emissions in the new parametrizations ( $954 \text{ Mg yr}^{-1}$ ) is similar to the predictions from two  
 75 GEOS-Chem studies<sup>11,12</sup> using the previous parametrization:  $860 \pm 440 \text{ Mg yr}^{-1}$  and  $910 \text{ Mg yr}^{-1}$ . The  
 76 spatial distribution of emissions (Fig. S2) shows a decrease in vegetated regions (e.g., the Amazon and  
 77 Congo rainforests) and an increase in regions with high soil  $\text{Hg}$  concentrations (e.g., eastern China).

78



79  
80 **Figure S2.** (a) Annual mean soil emissions of  $\text{Hg}^0$  with the new parametrization. (b) Difference  
81 between new and old (GEOS-Chem v12.8) soil emissions parametrizations (new minus old).  
82

### 83 **Section S2. Observational constraints on deforestation Hg fluxes**

84 There are several available sources of information that can be used to validate the deforestation  
85 emission factors (EF) calculated by GEOS-Chem (Fig. 1, SI Spreadsheet):  
86

87 1) *Soil Hg concentration measurements of paired forest-deforested sites:*

88 Previous studies have measured the concentrations of Hg soils at deforested sites ( $C_d$ ) and nearby  
89 forest ( $C_f$ ) plots. For this analysis, we assume that the difference in these soil concentrations is due to  
90 mainly the change in atmospheric exchange, which is supported by the magnitude of modeled erosion  
91 fluxes (Section S6) and available measurements<sup>5</sup>. We use the following equation to convert the  
92 difference in these concentrations to a deforestation emission factor of Hg in  $\text{Mg m}^{-2} \text{ yr}^{-1}$ :

$$93 \text{Total EF} = \frac{(C_d - C_f) \times \rho \times h}{t_d} \quad (\text{S3})$$

94 where  $\rho$  is the density of the soil,  $h$  is the depth of the soil layer, and  $t_d$  is the time since deforestation.  
95 In the US (Nearctic), there have been studies in Ohio<sup>13</sup> and Oregon<sup>14</sup> with measurements of Hg in  
96 deforested and forested soils, which we use to calculate deforestation EFs for the Nearctic. For the  
97 Amazon, more measurements are available (24 pairs of soil plots)<sup>8–10,15–25</sup>. We compiled a literature  
98 database of studies that compared Hg concentrations in deforested Amazonian soils with nearby forest  
99 plots (Fig. S3; SI Spreadsheet). Deforested sites show a consistent decrease compared to paired  
100 forested sites ( $p$ -value  $< 0.001$ ; Wilcoxon signed-rank test), with the median decrease being  $25 \text{ ng g}^{-1}$   
101 (10<sup>th</sup>–90<sup>th</sup> percentile:  $2$ – $58 \text{ ng g}^{-1}$ ). To calculate a deforestation EF for the Amazon, we apply this  
102 concentration decrease in Eq. S3 and assume an average Amazon soil density of  $1.25 \text{ ng g}^{-1}$ , a surface  
103 soil layer of 10 cm, and that deforested soils in the literature studies were measured 10 years after  
104 deforestation.

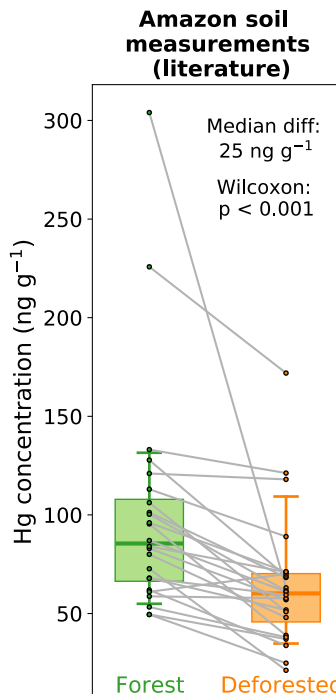


**Figure S3.** Measured Hg concentrations in forest (green) and deforested (orange) soils (0–20 cm depth) from the literature ( $n = 24$ )<sup>8–10,15–25</sup>. Box plots show the median values (solid lines), interquartile range (shaded), and 10<sup>th</sup> and 90<sup>th</sup> percentiles (whiskers). Gray lines connect paired sites from the same study. Listed  $p$ -value ( $<0.001$ ) refers to the Wilcoxon signed-rank test of the null hypothesis that paired forest and deforested sites come from the same distribution.

2) *Terrestrial-atmosphere exchange models validated by Hg observations:*

An estimate for the deforestation EF over China is available from the Wang et al.<sup>26</sup> modeling study. We use their area-averaged mean fluxes over forest and agricultural land cover to calculate a deforestation emission factor:

$$\text{Total EF} = (E_d - D_d) - (E_f - D_f) \quad (\text{S4})$$

where  $E_d$  and  $E_f$  are the terrestrial emission fluxes ( $\text{Mg m}^{-2} \text{ yr}^{-1}$ ) from Chinese agricultural land and forest, and  $D_d$  and  $D_f$  are the deposition fluxes ( $\text{Mg m}^{-2} \text{ yr}^{-1}$ ) to Chinese agricultural land and forest. Although this EF estimate is model-based, the Wang et al.<sup>26</sup> model was validated extensively with available terrestrial-atmosphere exchange measurements from China.

3) *Dynamic flux chamber measurements of forested and deforested soils:*

Additional studies investigating the impact of deforestation on atmospheric fluxes quantified the response of soil emissions using dynamic flux chamber measurements<sup>5,8–10,27,28</sup>. We compare these measurements to the soil-only EF modeled by GEOS-Chem. The soil emission factors measured by the studies is calculated as the difference between soil emissions ( $\text{Mg m}^{-2} \text{ yr}^{-1}$ ) over deforested and forested soils:

$$\text{Soil EF} = E_d - E_f \quad (\text{S5})$$

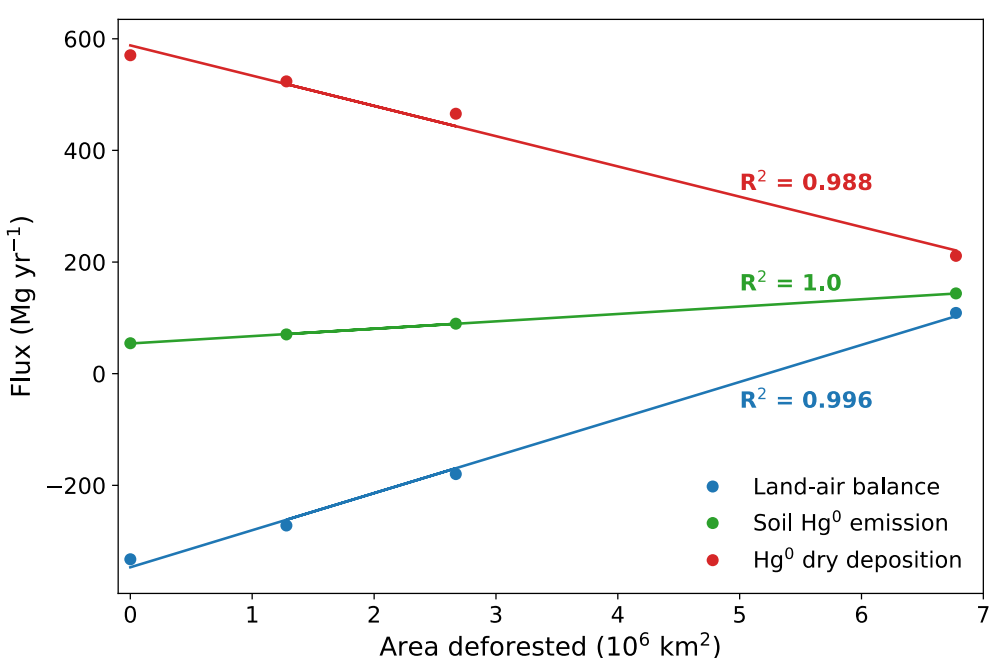
The comparison between GEOS-Chem simulated deforestation EFs and observation-derived values is summarized in Fig. 1. Observations are only available from three regions (Amazon, China and Nearctic). We found further references investigating the impact of deforestation on Hg for the Palaearctic region<sup>29,30</sup>, yet these focused on measuring Hg concentrations in aquatic media and methylation potential rather than soil concentrations or atmospheric exchange. Australian soil measurements<sup>31,32</sup> have been made before and after vegetation burning events, but do not cover the longer term soil Hg response to deforestation.

The modeled EF estimates and their uncertainties overlap with observation-derived EFs for all 3 regions. If anything, the modeled best estimate used in online simulations is conservative compared to

140 available observations, showing generally lower EFs (Fig. 1). However, it is unclear whether the  
 141 sparse observations available are representative of the overall region. The modeled EF uncertainty  
 142 estimates cover 1–2 orders of magnitude, emphasizing the current uncertainties in the response of Hg  
 143 fluxes to deforestation. Figure 1 also reveals the regions where no observations of the impact of  
 144 deforestation on Hg cycling are currently available. Specifically, the Afrotropic and Indomalayan  
 145 domains would be priorities for future measurement campaigns, given the current impact of  
 146 deforestation in those regions (Fig. 2). It remains unknown whether Southeast Asian and African  
 147 rainforests show similarly high levels of Hg in litterfall as the Amazon rainforest<sup>33</sup>.  
 148

#### 149 Section S3. Global deforestation-driven emissions estimates

150 We use perturbation simulations in which a set area within each region is deforested to calculate each  
 151 deforestation EF. In the EF approach, we assume that 1) land-air fluxes respond linearly to deforested  
 152 area and 2) spatial variability in the deforestation response within regions can be ignored. We explored  
 153 the validity these assumptions using the four Amazon deforestation scenario simulations conducted in  
 154 this work (Fig. S4). In the Amazon simulations — the reference simulation with 2003 forest cover  
 155 (HIST), governance scenario for 2050 (GOV), business-as-usual for 2050 (BAU), and savannization  
 156 (SAV) — different areas (both in spatial pattern and extent) were deforested in the Amazon region.  
 157 The total fluxes from the Amazon basin for Hg<sup>0</sup> dry deposition, soil Hg<sup>0</sup> emissions, and the overall  
 158 land-air balance of Hg all respond linearly ( $R^2 > 0.98$ ) to the magnitude of the deforested area.  
 159 Therefore, the approach of calculating deforestation EFs and scaling these with deforested areas would  
 160 likely not be highly sensitive to the spatial distribution and amount of deforestation. Therefore, we  
 161 conducted 7 other idealized deforestation simulations for the other land regions (Fig. S5).  
 162



163  
 164 **Figure S4.** Relationship between land-air fluxes and the area deforested in GEOS-Chem simulations  
 165 for the Amazon rainforest. Fluxes are averaged over the Amazon rainforest domain and listed  $R^2$   
 166 values refer to linear models.  
 167

168 Additional data related to the calculation of historical deforestation-driven emissions of Hg are  
 169 presented in this section. The maps defining the regions used in this study is shown in Fig. S5. Table  
 170 S3 tabulates the results from the perturbation simulations for the different regions and the resultant  
 171 emission factors. Fig. S6 explores the impact of choosing different time horizons for the deforestation  
 172 area on the calculated Hg emissions globally and by country. Fig. S7 shows the map of Hg  
 173 deforestation-driven emissions, assuming a 45 year time horizon (deforestation area of 1970–2014  
 174 from the LUH2 dataset<sup>34</sup>).  
 175

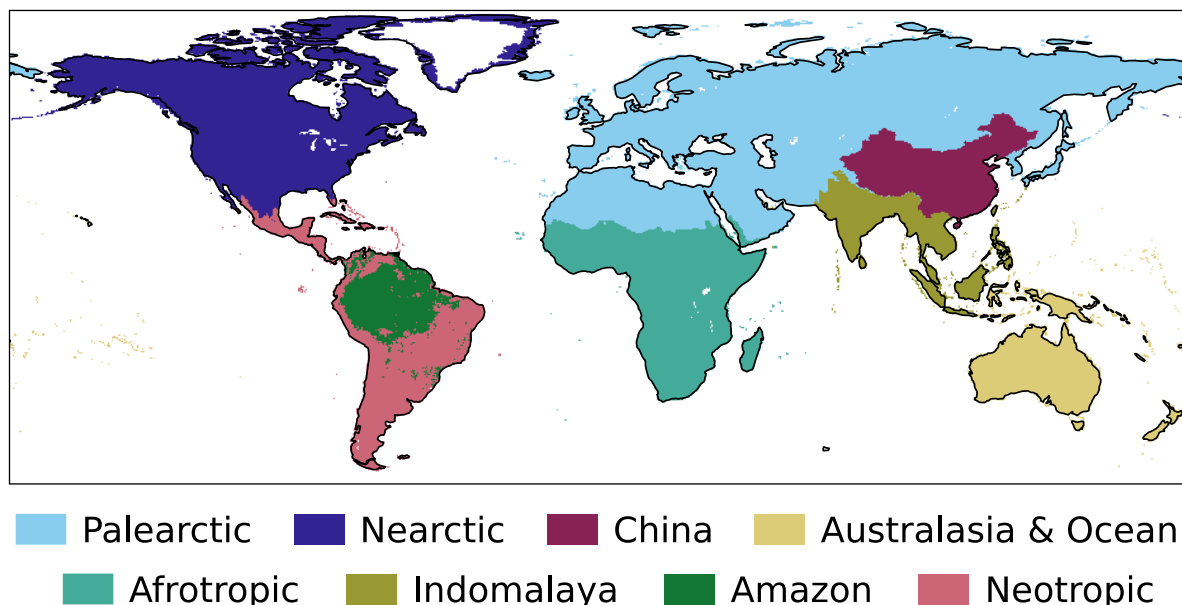
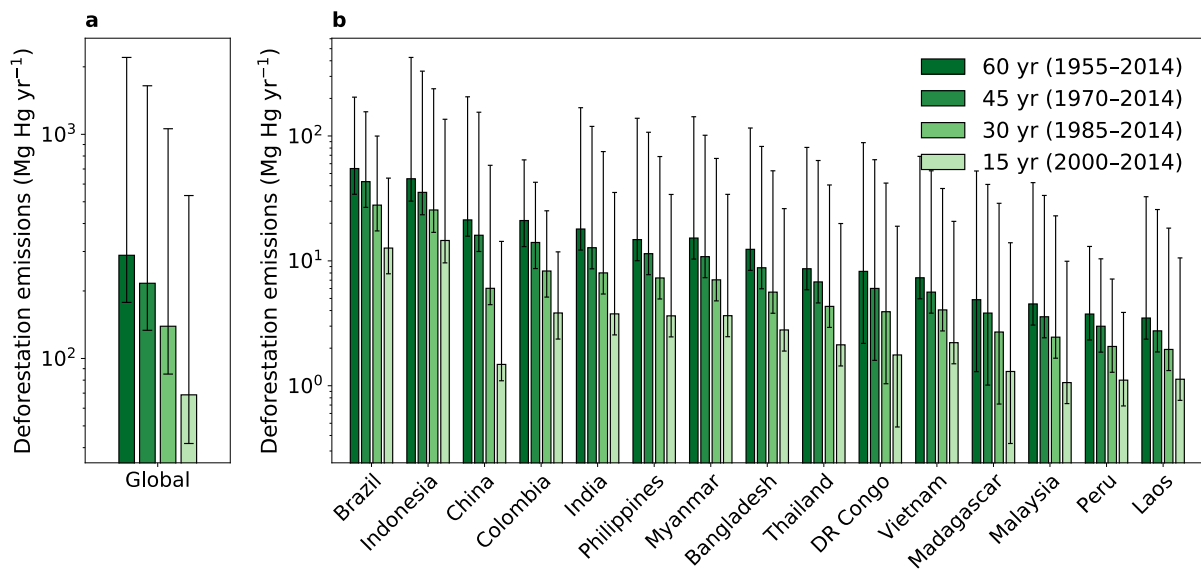


**Figure S5.** Definition of regions used to calculate the deforestation emission factors.

**Table S3.** Results from the deforestation perturbation simulations in GEOS-Chem for determining the response of land-air fluxes to deforesting a specified area. Emissions factors are listed with the 95% confidence interval calculated in offline simulations assessing the uncertainties due to model parameters (Section S4).

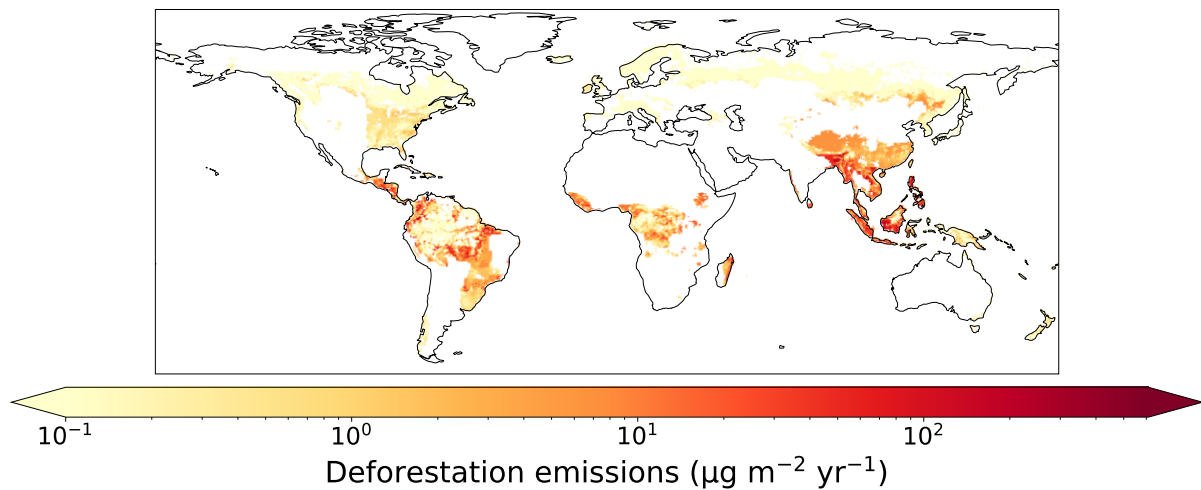
Realm	Area deforested (km <sup>2</sup> )	Change in emissions (Mg yr <sup>-1</sup> )	Change in deposition (Mg yr <sup>-1</sup> )	Change in net emissions (Mg yr <sup>-1</sup> )	Emissions factor (Mg m <sup>-2</sup> yr <sup>-1</sup> ) [95% confidence interval]
Afrotropic	3 644 969	29.1	-10.0	39.1	$1.1 \times 10^{-5}$ [ $2.8 \times 10^{-6}$ to $1.2 \times 10^{-4}$ ]
Neotropic	2 422 577	13.0	-4.9	17.9	$7.4 \times 10^{-6}$ [ $4.8 \times 10^{-6}$ to $5.7 \times 10^{-5}$ ]
Indomalaya	2 626 474	31.6	-28.3	59.9	$2.3 \times 10^{-5}$ [ $1.5 \times 10^{-5}$ to $2.1 \times 10^{-4}$ ]
Palearctic	4 221 663	5.8	-4.3	10.1	$2.4 \times 10^{-6}$ [ $7.6 \times 10^{-8}$ to $2.3 \times 10^{-5}$ ]
Nearctic	4 606 898	31.6	-17.4	48.9	$1.1 \times 10^{-5}$ [ $7.1 \times 10^{-6}$ to $6.2 \times 10^{-5}$ ]
Australasia	1 088 250	1.9	-4.8	6.6	$6.1 \times 10^{-6}$ [ $8.3 \times 10^{-7}$ to $5.4 \times 10^{-5}$ ]
China	1 141 180	16.6	-10.1	26.7	$2.3 \times 10^{-5}$ [ $1.7 \times 10^{-5}$ to $2.3 \times 10^{-4}$ ]
Amazon	6 775 429	96.2	-394.0	490.2	$7.2 \times 10^{-5}$ [ $4.5 \times 10^{-5}$ to $2.0 \times 10^{-4}$ ]



186

187 **Figure S6.** (a) Global and (b) country-level deforestation emissions of Hg for the top 15 emitting  
188 countries. Results are summarized accumulating deforested area over different time horizons (15  
189 years, 30 years, 45 years, and 60 years) before 2015. Error bars refer to the 95% confidence interval  
190 based on the uncertainty in model parameters (Section S4).

191



192

193 **Figure S7.** Map of net emissions of Hg from deforestation calculated over a 45 year time horizon  
194 before 2015 (1970-2014), using deforested area from the LUH2 dataset<sup>34</sup>.

195

196

197 **Section S4. Model uncertainty analysis**

198

199

**Table S4.** Parameter uncertainty bounds applied in the uncertainty analysis.

Parameter	Min	Max	Units	Distribution	Comment
Soil emission parametrization	1	100	-	Uniform	Integer representing one of 100 reasonable parametrizations calculated within the range of observed uncertainties (Table S5)
Percentile of replaced LAI when building scenarios	10	90	-	Uniform	e.g., deforested Amazon area is assigned 10 <sup>th</sup> percentile LAI of HIST savanna, instead of mean for default estimate
Dry deposition Hg <sup>0</sup> reactivity ( $f_0$ ) Amazon rainforest	10 <sup>-2</sup>	0.5	-	Loguniform	Based on Feinberg et al. <sup>33</sup> , within range of available vegetation uptake measurements
Dry deposition Hg <sup>0</sup> reactivity ( $f_0$ ) other rainforests	10 <sup>-5</sup>	0.2	-	Loguniform	Based on Feinberg et al. <sup>33</sup> ; no available measurements from other rainforests, leading to wider $f_0$ uncertainty
Dry deposition Hg <sup>0</sup> reactivity ( $f_0$ ) elsewhere	10 <sup>-5</sup>	$5 \times 10^{-5}$	-	Uniform	Based on Feinberg et al. <sup>33</sup> , within range of available vegetation uptake measurements
Biomass burning emission factor for Amazon	350	615	$\mu\text{g m}^{-2}$	Uniform	Estimated range in literature <sup>10,35,36</sup>

200

201

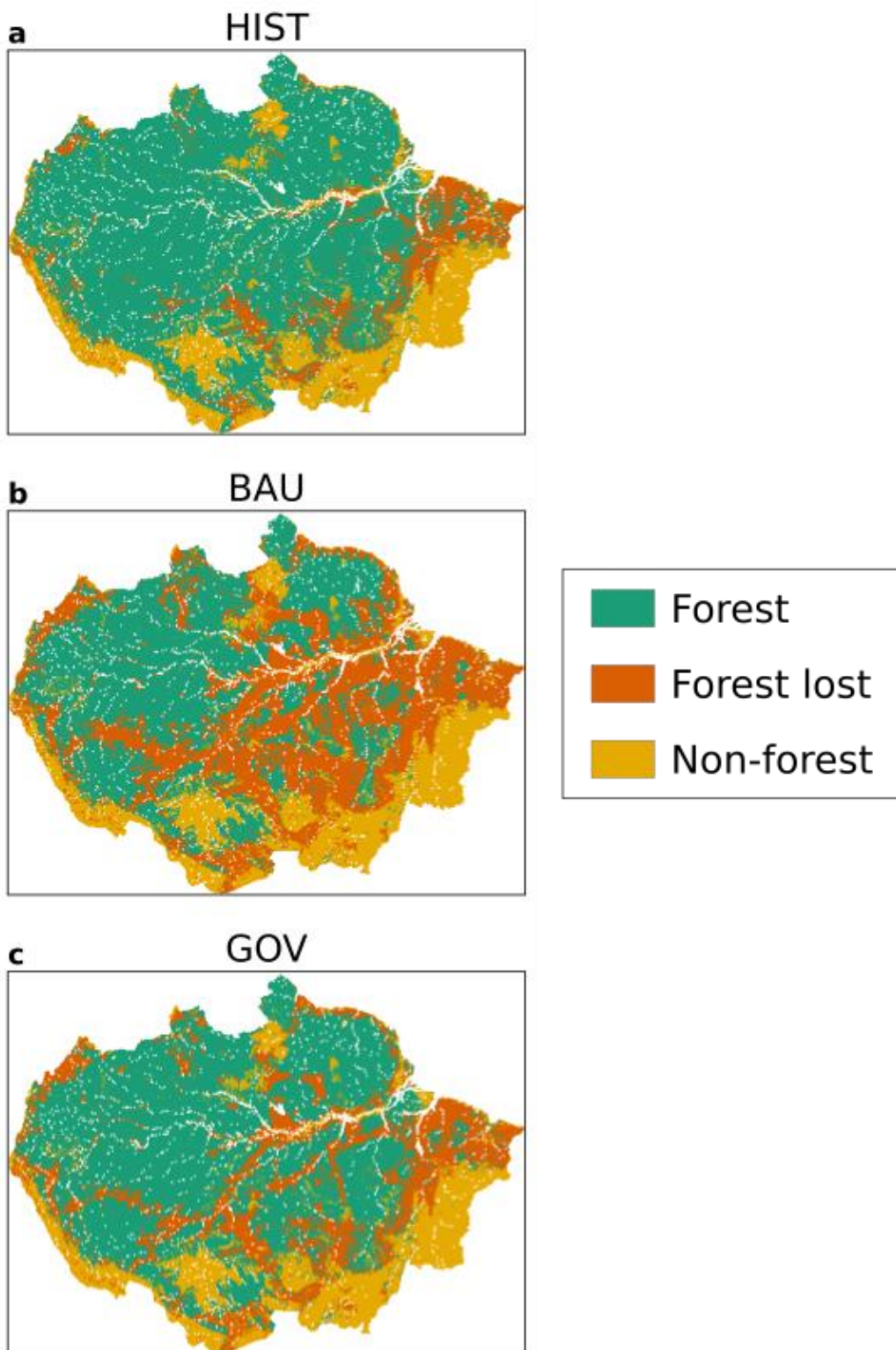
**Table S5.** Bounds of observed parameters used to calculate 100 reasonable soil emission parametrizations, which are then applied in the uncertainty analysis (Table S4).

Parameter	Min	Max	Units	Comment
Ratio of deforested to forested Amazon soil emissions	1.8	31	-	Range from Table S1
Ratio of Amazon to extratropical soil emissions	3.5	8	-	Assume 50% error from Table S2
Extratropical grassland soil emissions	3.5	11.4	$\mu\text{g m}^{-2} \text{ yr}^{-1}$	Grasslands and background soil range from literature reviews <sup>6,7</sup>
Deforested Amazon soil emissions	9.8	79	$\mu\text{g m}^{-2} \text{ yr}^{-1}$	Range from Table S1

204

205

206 Section S5. Scenarios for Amazon deforestation and global reforestation

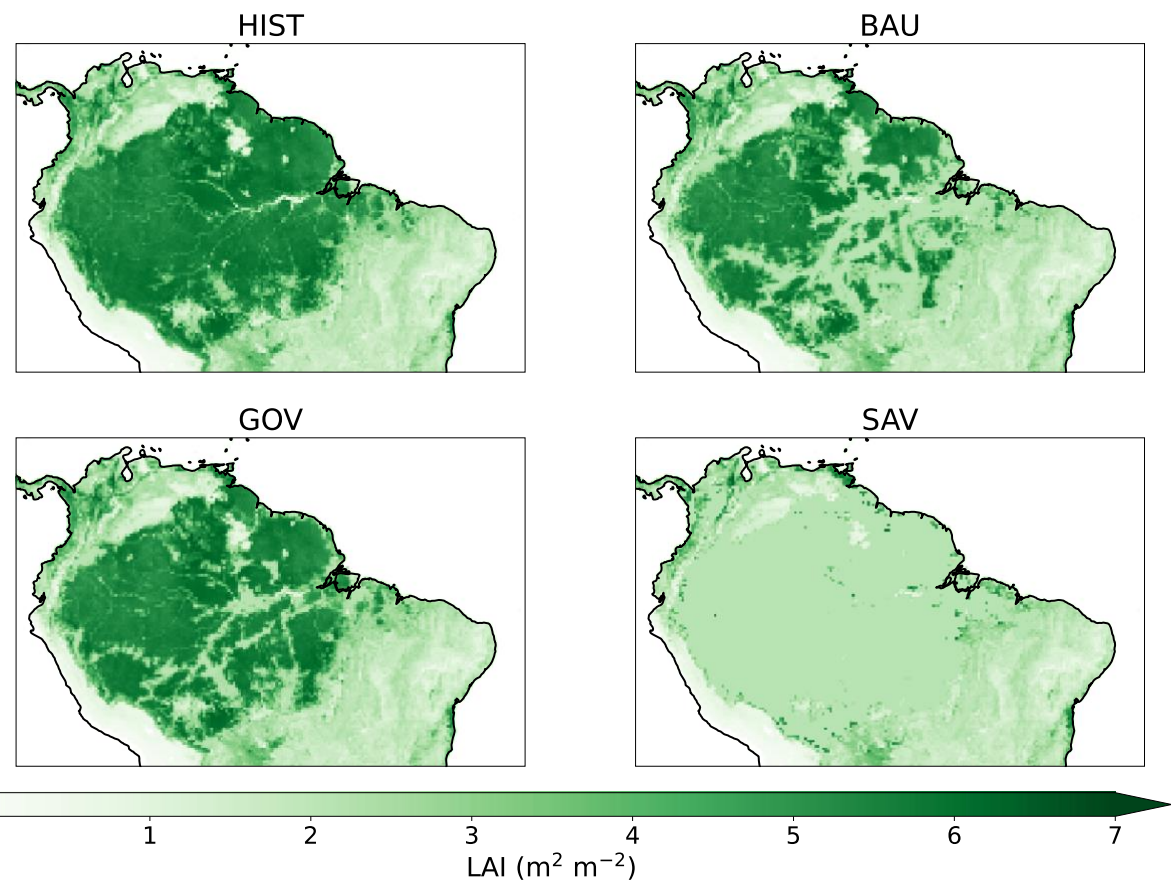


207

208 **Figure S8.** Map of the Amazon basin showing the area of forest, forest loss and rangeland and  
209 agriculture in (a) HIST; and projections for 2050 in (b) Business as Usual (BAU) and (c) Governance  
210 (GOV) scenarios (replotted from Soares-Filho et al.<sup>37</sup> data).

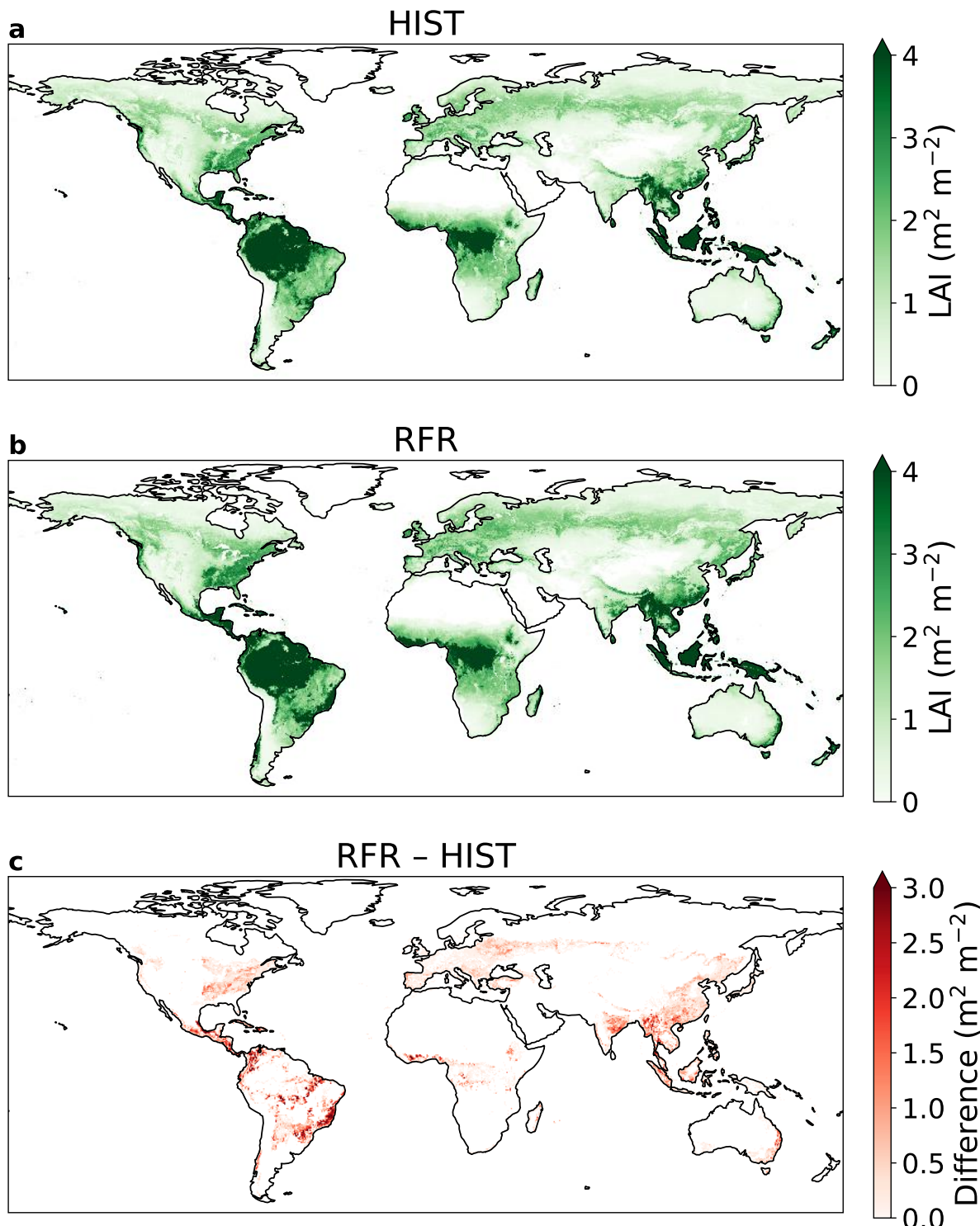
211

212



213

214 **Figure S9.** Annual mean leaf area index (LAI) maps for the Amazon deforestation scenarios at  $0.25^\circ$   
215  $\times 0.25^\circ$  resolution. The simulations names refer to the following scenarios: reference (HIST),  
216 Governance (GOV), and Savannization (SAV).



217

218 **Figure S10.** Annual mean leaf area index (LAI) maps at  $0.25 \times 0.25^\circ$  resolution for: (a) the reference  
 219 (HIST) scenario (b) Reforestation scenario (RFR) (c) Difference between RFR and HIST.

220

221 **Section S6. Impact of Amazon deforestation on erosion**

222 Previous field studies<sup>15,38</sup> have suggested that erosion of Hg is increased after deforestation in the  
 223 Amazon, measuring enhanced runoff of Hg in deforested catchments. We estimated the change in soil  
 224 displacement by water erosion (soil erosion) in the Amazon deforestation scenarios using the RUSLE-  
 225 based<sup>39</sup> modeling platform Global Soil Erosion Modeling (GloSEM)<sup>40,41</sup>. As a detachment-limited soil  
 226 erosion prediction model, GloSEM estimates soil erosion (expressed as a mass of soil lost per unit area  
 227 and time,  $\text{Mg ha}^{-1} \text{yr}^{-1}$ ) due to inter-rill and rill erosion processes by multiplication of six contributing

228 factors. The modeling scheme follows the same principle of most RUSLE-type models or more  
 229 complex catchment-scale process-based models, with a driving force (erosivity of the climate, R), a  
 230 resistance term (erodibility of the soil, K) and other factors representing the farming choice, i.e.,  
 231 topographical conformation of the field (LS), cropping system (C), and soil conservation practices (P).  
 232

233 Our approach for calculating soil erosion in the Amazon scenarios is similar to the GloSEM  
 234 parametrization adopted by Borrelli et al.<sup>40,41</sup> to estimate human-induced soil erosion change between  
 235 2001 and 2070 at a global scale. The horizontal resolution of the native soil erosion modeling is 250 ×  
 236 250 m. The calculation of erosivity (R), erodibility (K), topographical conformation of the field (LS),  
 237 and soil conservation practices (P) factors are described in Borrelli et al.<sup>40,41</sup>. We acknowledge that the  
 238 calculation of erosion model factors for the Amazon rainforest may be associated with higher  
 239 uncertainties than other regions due to the lower density in meteorological stations<sup>42</sup> and soil sampling  
 240 sites<sup>43</sup>. For this study, we adapted the computation of the land cover and management factor (C-  
 241 factor), which measures the combined effect of vegetation cover and cropping system variables on the  
 242 soil erosion process. We parametrize the C-factor according to two layers of information: 1) the spatial  
 243 dimension of land use classes according to the deforestation scenarios from Soares-Filho et al.<sup>37</sup>  
 244 (described below); 2) the vegetation condition in each land use class using the MODIS MOD44B  
 245 Vegetation Continuous Fields product (VCF) (~250m spatial resolution) as a proxy to quantify (i)  
 246 surface vegetation cover, (ii) tree cover, and (iii) bare soil. As we focus our analysis on comparing the  
 247 forest coverage in the years 2003 and 2050, the baseline vegetation condition is given by the average  
 248 VCF values over the years 2000, 2001 and 2002. The C-factor for noncropland areas ( $C_{nc}$ ) is estimated  
 249 in two steps. First, a preliminary C-factor ( $C_p$ ) not considering tree cover is calculated as:  
 250

$$C_p = C_{min} + ((C_{max} - C_{min}) NVS) \quad (S6)$$

251 where the  $C_{min}$  (0.01) and  $C_{max}$  (0.15) express the potential range in C-factor values for dense to  
 252 sparse grassland cover. NVS (non-vegetated surface) is spatially defined using the MODIS MOD44B  
 253 VCF data normalized to a range from 0 to 1 and describes the percentage of ground covered by any  
 254 vegetation type. For the NVS, the C-factor is set to 0.5. Within the next step, the final land cover and  
 255 management C-factor for non-croplands ( $C_{nc}$ ) is computed including the tree coverage (TC) defined  
 256 using the MODIS MOD44B VCF normalized to range from 0 to 1:  
 257

$$C_{nc} = C_p \min + ((C_p \max - C_p \min) TC) \quad (S7)$$

258 where the  $C_p \min$  and  $C_p \max$  values are set to 0.0001 (100% canopy cover) and 0.009 (sparse forest  
 259 vegetation).  
 260

261 While the deforestation scenarios proposed by Soares-Filho et al.<sup>37</sup> provide a spatial quantification of  
 262 the forest losses between 2003 and 2050, the annual shares of conversion from forest to grassland or  
 263 cropland are separate from the annual projection of the Land-Use Harmonization (LUH2) data<sup>34</sup>,  
 264 which provides fractional land-use patterns (850-2100) at 0.25° × 0.25° resolution. The downscaling  
 265 of the LUH2 fractional cropland and grassland data from 0.25° × 0.25° resolution to the 250 m × 250  
 266 m resolution of the erosion model is performed through a probabilistic land use allocation scheme  
 267 based on classification rules applied to auxiliary information (i.e., a crop suitability index, more detail  
 268 in Borrelli et al.<sup>40</sup>). Finally, the C-factor of the cropland is defined at sub-national administrative level  
 269 (Global Administrative Unit Levels) based on the Food and Agriculture Organization's (FAO)  
 270 FAOSTAT database, which allowed to statistically describe typical crop rotations in each region. The  
 271 C-factor of the croplands ranges from 0.131 (Northern Suriname) to 0.332 (Northeast Brazil).  
 272

273 Following the assumption of Lugato et al.<sup>44</sup> for eroded carbon, we assume that 30% of the eroded soil  
 274 flux is not redeposited on land and enters riverine systems. The fraction of eroded Hg which enters  
 275 aquatic systems is uncertain, depending on hillslopes dynamics and flow patterns that are not  
 276 explicitly modeled by the RUSLE-based framework, as well as whether Hg would be selectively  
 277 eroded relative to carbon. We recognize that this assumption introduces uncertainty into our  
 278 calculations, and assume that the fraction of eroded soil which enters riverine systems can vary  
 279 between 5–47%, the range reported by Van Oost et al.<sup>45</sup> We calculate the eroded flux of Hg from land  
 280 by multiplying the soil flux by the median Hg concentration in Amazon forested soils from a literature  
 281 review (86 ng g<sup>-1</sup>; see SI Spreadsheet).  
 282

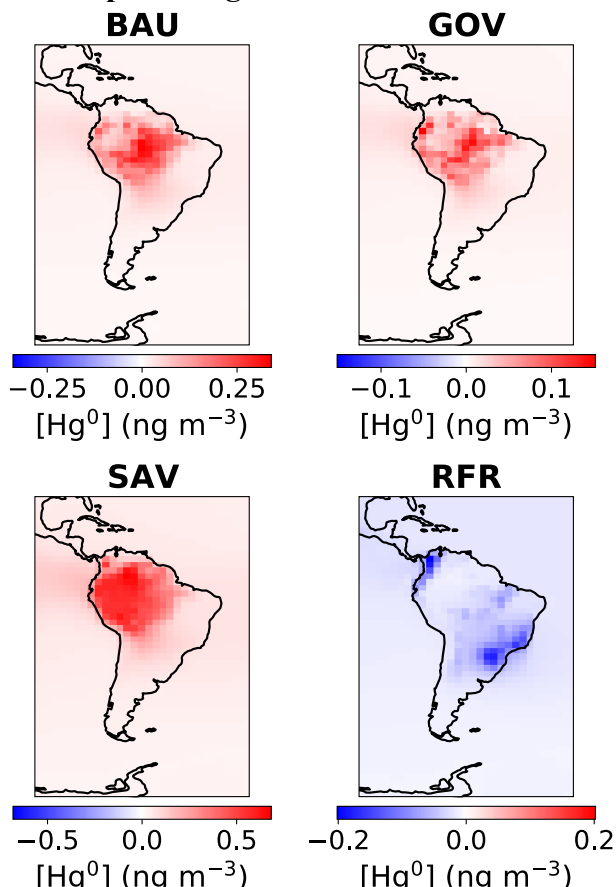
283 For each Amazon scenario, we tabulate the Hg erosion fluxes in Table S6. Erosion in the HIST  
 284 scenario represents a flux of 64 Mg yr<sup>-1</sup> (uncertainty range: 11–100 Mg yr<sup>-1</sup>). Erosion is enhanced in  
 285 the deforestation scenarios, ranging from +14% increase in GOV to a 96% increase in the extreme  
 286 SAV scenario. The absolute magnitudes of erosion flux changes are smaller than the perturbations in  
 287 the land-air flux, driven by changes in Hg<sup>0</sup> soil emissions and dry deposition (Table S6). Overall,  
 288 perturbations to the erosion flux are approximately 14% of the perturbations to the land-air flux due to  
 289 deforestation. A previous field study<sup>5</sup> has also suggested that the majority of flux changes after  
 290 deforestation occurs through atmospheric exchange (97%) rather than erosion to riverine systems.  
 291 Therefore, the land-air changes to the fluxes play the larger role in the impact of deforestation on the  
 292 mass balance of Hg in soils. Nevertheless, changes to erosion will affect downstream Hg  
 293 concentrations and the methylation potential after deforestation<sup>5,29</sup>, which would be important to  
 294 consider when assessing the impact of deforestation on local ecosystems.  
 295

296 **Table S6.** Soil erosion fluxes for the Amazon basin calculated by the erosion model GloSEM. The  
 297 simulations names refer to the following scenarios: reference (HIST), Business-as-usual (BAU),  
 298 Governance (GOV), and Savannization (SAV).

Scenario	HIST	BAU	GOV	SAV
Soil loss (Mt yr <sup>-1</sup> )	2467	3276	2816	4834
30% of soil loss (Mt yr <sup>-1</sup> ) <sup>a</sup>	740	983	845	1450
[5%–47%]	[123–1159]	[164–1540]	[141–1323]	[242–2272]
Hg erosion (Mg yr <sup>-1</sup> )	64	85	73	125
[uncertainty range]	[11–100]	[14–132]	[12–114]	[21–195]
Change from HIST (Mg yr <sup>-1</sup> )	-	21	9	61
(relative change)		(+33%)	(+14%)	(+96%)
Land-air flux change from HIST (Mg yr <sup>-1</sup> )	-	153	61	441

299 <sup>a</sup> This is the flux assumed to be entering riverine systems

300  
 301

302 **Section S7. Impacts on atmospheric Hg concentrations**

303

304 **Figure S11.** Annual mean differences in simulated atmospheric  $\text{Hg}^0$  concentration at the surface  
 305 between scenarios — Business-as-usual (BAU), Governance (GOV), Savannization (SAV), and global  
 306 reforestation (RFR) — and the HIST reference simulation.

307

308 **Supplementary References**

309 (1) Khan, T. R.; Obrist, D.; Agnan, Y.; Selin, N. E.; Perlinder, J. A. Atmosphere-Terrestrial Exchange  
 310 of Gaseous Elemental Mercury: Parameterization Improvement through Direct Comparison with  
 311 Measured Ecosystem Fluxes. *Environ. Sci.: Processes Impacts* **2019**, *21* (10), 1699–1712.  
 312 <https://doi.org/10.1039/C9EM00341J>.

313 (2) Selin, N. E.; Jacob, D. J.; Yantosca, R. M.; Strode, S.; Jaeglé, L.; Sunderland, E. M. Global 3-D  
 314 Land-Ocean-Atmosphere Model for Mercury: Present-Day versus Preindustrial Cycles and  
 315 Anthropogenic Enrichment Factors for Deposition. *Global Biogeochem. Cycles* **2008**, *22* (2),  
 316 GB2011. <https://doi.org/10.1029/2007GB003040>.

317 (3) Verstraete, M. M. Radiation Transfer in Plant Canopies: Transmission of Direct Solar Radiation  
 318 and the Role of Leaf Orientation. *J. Geophys. Res.* **1987**, *92* (D9), 10985.  
 319 <https://doi.org/10.1029/JD092iD09p10985>.

320 (4) Zhou, J.; Wang, Z.; Zhang, X.; Driscoll, C. T.; Lin, C.-J. Soil-Atmosphere Exchange Flux of  
 321 Total Gaseous Mercury (TGM) at Subtropical and Temperate Forest Catchments. *Atmos. Chem.  
 322 Phys.* **2020**, *20* (24), 16117–16133. <https://doi.org/10.5194/acp-20-16117-2020>.

323 (5) Eckley, C. S.; Eagles-Smith, C.; Tate, M. T.; Krabbenhoft, D. P. Surface-Air Mercury Fluxes and  
 324 a Watershed Mass Balance in Forested and Harvested Catchments. *Environmental Pollution*  
 325 **2021**, *277*, 116869. <https://doi.org/10.1016/j.envpol.2021.116869>.

326 (6) Zhu, W.; Lin, C.-J.; Wang, X.; Sommar, J.; Fu, X.; Feng, X. Global Observations and Modeling  
 327 of Atmosphere-Surface Exchange of Elemental Mercury: A Critical Review. *Atmos. Chem.  
 328 Phys.* **2016**, *16* (7), 4451–4480. <https://doi.org/10.5194/acp-16-4451-2016>.

329 (7) Agnan, Y.; Le Dantec, T.; Moore, C. W.; Edwards, G. C.; Obrist, D. New Constraints on  
330 Terrestrial Surface–Atmosphere Fluxes of Gaseous Elemental Mercury Using a Global  
331 Database. *Environ. Sci. Technol.* **2016**, *50* (2), 507–524. <https://doi.org/10.1021/acs.est.5b04013>.

332 (8) Magarelli, G.; Fostier, A. Influence of Deforestation on the Mercury Air/Soil Exchange in the  
333 Negro River Basin, Amazon. *Atmos. Environ.* **2005**, *39* (39), 7518–7528.  
334 <https://doi.org/10.1016/j.atmosenv.2005.07.067>.

335 (9) Almeida, M. D.; Marins, R. V.; Paraquetti, H. H. M.; Bastos, W. R.; Lacerda, L. D. Mercury  
336 Degassing from Forested and Open Field Soils in Rondônia, Western Amazon, Brazil.  
337 *Chemosphere* **2009**, *77* (1), 60–66. <https://doi.org/10.1016/j.chemosphere.2009.05.018>.

338 (10) Carpi, A.; Fostier, A. H.; Orta, O. R.; dos Santos, J. C.; Gittings, M. Gaseous Mercury Emissions  
339 from Soil Following Forest Loss and Land Use Changes: Field Experiments in the United States  
340 and Brazil. *Atmos. Environ.* **2014**, *96*, 423–429. <https://doi.org/10.1016/j.atmosenv.2014.08.004>.

341 (11) Song, S.; Selin, N. E.; Soerensen, A. L.; Angot, H.; Artz, R.; Brooks, S.; Brunke, E.-G.; Conley,  
342 G.; Dommergue, A.; Ebinghaus, R.; Holsen, T. M.; Jaffe, D. A.; Kang, S.; Kelley, P.; Luke, W.  
343 T.; Magand, O.; Marumoto, K.; Pfaffhuber, K. A.; Ren, X.; Sheu, G.-R.; Slemr, F.; Warneke, T.;  
344 Weigelt, A.; Weiss-Penzias, P.; Wip, D. C.; Zhang, Q. Top-down Constraints on Atmospheric  
345 Mercury Emissions and Implications for Global Biogeochemical Cycling. *Atmos. Chem. Phys.*  
346 **2015**, *15* (12), 7103–7125. <https://doi.org/10.5194/acp-15-7103-2015>.

347 (12) Horowitz, H. M.; Jacob, D. J.; Zhang, Y.; Dibble, T. S.; Slemr, F.; Amos, H. M.; Schmidt, J. A.;  
348 Corbitt, E. S.; Marais, E. A.; Sunderland, E. M. A New Mechanism for Atmospheric Mercury  
349 Redox Chemistry: Implications for the Global Mercury Budget. *Atmos. Chem. Phys.* **2017**, *17*  
350 (10), 6353–6371. <https://doi.org/10.5194/acp-17-6353-2017>.

351 (13) Gamby, R. L.; Hammerschmidt, C. R.; Costello, D. M.; Lamborg, C. H.; Runkle, J. R.  
352 Deforestation and Cultivation Mobilize Mercury from Topsoil. *Science of The Total  
353 Environment* **2015**, *532*, 467–473. <https://doi.org/10.1016/j.scitotenv.2015.06.025>.

354 (14) Homann, P. S.; Derbyshire, R. L.; Bormann, B. T.; Morrisette, B. A. Forest Structure Affects  
355 Soil Mercury Losses in the Presence and Absence of Wildfire. *Environ. Sci. Technol.* **2015**, *49*  
356 (21), 12714–12722. <https://doi.org/10.1021/acs.est.5b03355>.

357 (15) Fostier, A. H.; Forti, M. C.; Guimarães, J. R.; Melfi, A. J.; Boulet, R.; Espírito Santo, C. M.;  
358 Krug, F. J. Mercury Fluxes in a Natural Forested Amazonian Catchment (Serra Do Navio,  
359 Amapá State, Brazil). *Sci. Total Environ.* **2000**, *260* (1–3), 201–211.  
360 [https://doi.org/10.1016/S0048-9697\(00\)00564-7](https://doi.org/10.1016/S0048-9697(00)00564-7).

361 (16) Gerson, J. R.; Szponar, N.; Zambrano, A. A.; Bergquist, B.; Broadbent, E.; Driscoll, C. T.;  
362 Erkenswick, G.; Evers, D. C.; Fernandez, L. E.; Hsu-Kim, H.; Inga, G.; Lansdale, K. N.;  
363 Marchese, M. J.; Martinez, A.; Moore, C.; Pan, W. K.; Purizaca, R. P.; Sánchez, V.; Silman, M.;  
364 Ury, E. A.; Vega, C.; Watsa, M.; Bernhardt, E. S. Amazon Forests Capture High Levels of  
365 Atmospheric Mercury Pollution from Artisanal Gold Mining. *Nat Commun* **2022**, *13* (1), 559.  
366 <https://doi.org/10.1038/s41467-022-27997-3>.

367 (17) Almeida, M. D.; Lacerda, L. D.; Bastos, W. R.; Herrmann, J. C. Mercury Loss from Soils  
368 Following Conversion from Forest to Pasture in Rondônia, Western Amazon, Brazil.  
369 *Environmental Pollution* **2005**, *137* (2), 179–186. <https://doi.org/10.1016/j.envpol.2005.02.026>.

370 (18) Lacerda, L. D.; de Souza, M.; Ribeiro, M. G. The Effects of Land Use Change on Mercury  
371 Distribution in Soils of Alta Floresta, Southern Amazon. *Environmental Pollution* **2004**, *129* (2),  
372 247–255. <https://doi.org/10.1016/j.envpol.2003.10.013>.

373 (19) Béliveau, A.; Lucotte, M.; Davidson, R.; do Canto Lopes, L. O.; Paquet, S. Early Hg Mobility in  
374 Cultivated Tropical Soils One Year after Slash-and-Burn of the Primary Forest, in the Brazilian  
375 Amazon. *Science of The Total Environment* **2009**, *407* (15), 4480–4489.  
376 <https://doi.org/10.1016/j.scitotenv.2009.04.012>.

377 (20) Béliveau, A.; Lucotte, M.; Davidson, R.; Paquet, S.; Mertens, F.; Passos, C. J.; Romana, C. A.  
378 Reduction of Soil Erosion and Mercury Losses in Agroforestry Systems Compared to Forests  
379 and Cultivated Fields in the Brazilian Amazon. *Journal of Environmental Management* **2017**,  
380 *203*, 522–532. <https://doi.org/10.1016/j.jenvman.2017.07.037>.

381 (21) Patry, C.; Davidson, R.; Lucotte, M.; Béliveau, A. Impact of Forested Fallows on Fertility and  
382 Mercury Content in Soils of the Tapajós River Region, Brazilian Amazon. *Science of The Total  
383 Environment* **2013**, *458–460*, 228–237. <https://doi.org/10.1016/j.scitotenv.2013.04.037>.

384 (22) Comte, I.; Lucotte, M.; Davidson, R.; Reis de Carvalho, C. J.; de Assis Oliveira, F.; Rousseau, G.  
 385 X. Impacts of Land Uses on Mercury Retention in Long-Time Cultivated Soils, Brazilian  
 386 Amazon. *Water Air Soil Pollut.* **2013**, *224* (4), 1515. <https://doi.org/10.1007/s11270-013-1515-3>.

387 (23) Mainville, N.; Webb, J.; Lucotte, M.; Davidson, R.; Betancourt, O.; Cueva, E.; Mergler, D.  
 388 Decrease of Soil Fertility and Release of Mercury Following Deforestation in the Andean  
 389 Amazon, Napo River Valley, Ecuador. *Science of The Total Environment* **2006**, *368* (1), 88–98.  
 390 <https://doi.org/10.1016/j.scitotenv.2005.09.064>.

391 (24) Roulet, M.; Lucotte, M.; Saint-Aubin, A.; Tran, S.; Rhéault, I.; Farella, N.; De Jesus Da silva, E.;  
 392 Dezencourt, J.; Sousa Passos, C.-J.; Santos Soares, G.; Guimarães, J.-R. D.; Mergler, D.;  
 393 Amorim, M. The Geochemistry of Mercury in Central Amazonian Soils Developed on the Alter-  
 394 Do-Chão Formation of the Lower Tapajós River Valley, Pará State, Brazil. *Science of The Total  
 395 Environment* **1998**, *223* (1), 1–24. [https://doi.org/10.1016/S0048-9697\(98\)00265-4](https://doi.org/10.1016/S0048-9697(98)00265-4).

396 (25) Wasserman, J. C.; Campos, R. C.; Hacon, S. de S.; Farias, R. A.; Caires, S. M. Mercury in Soils  
 397 and Sediments from Gold Mining Liabilities in Southern Amazonia. *Quím. Nova* **2007**, *30* (4).  
 398 <https://doi.org/10.1590/S0100-40422007000400003>.

399 (26) Wang, X.; Lin, C.-J.; Yuan, W.; Sommar, J.; Zhu, W.; Feng, X. Emission-Dominated Gas  
 400 Exchange of Elemental Mercury Vapor over Natural Surfaces in China. *Atmos. Chem. Phys.*  
 401 **2016**, *16* (17), 11125–11143. <https://doi.org/10.5194/acp-16-11125-2016>.

402 (27) Mazur, M.; Mitchell, C. P. J.; Eckley, C. S.; Eggert, S. L.; Kolka, R. K.; Sebestyen, S. D.; Swain,  
 403 E. B. Gaseous Mercury Fluxes from Forest Soils in Response to Forest Harvesting Intensity: A  
 404 Field Manipulation Experiment. *Science of The Total Environment* **2014**, *496*, 678–687.  
 405 <https://doi.org/10.1016/j.scitotenv.2014.06.058>.

406 (28) Ma, M.; Wang, D.; Sun, R.; Shen, Y.; Huang, L. Gaseous Mercury Emissions from Subtropical  
 407 Forested and Open Field Soils in a National Nature Reserve, Southwest China. *Atmospheric  
 408 Environment* **2013**, *64*, 116–123. <https://doi.org/10.1016/j.atmosenv.2012.09.038>.

409 (29) Eklöf, K.; Lidskog, R.; Bishop, K. Managing Swedish Forestry's Impact on Mercury in Fish:  
 410 Defining the Impact and Mitigation Measures. *Ambio* **2016**, *45* (S2), 163–174.  
 411 <https://doi.org/10.1007/s13280-015-0752-7>.

412 (30) De Wit, H. A.; Granhus, A.; Lindholm, M.; Kainz, M. J.; Lin, Y.; Braaten, H. F. V.; Blaszcak, J.  
 413 Forest Harvest Effects on Mercury in Streams and Biota in Norwegian Boreal Catchments.  
 414 *Forest Ecology and Management* **2014**, *324*, 52–63.  
 415 <https://doi.org/10.1016/j.foreco.2014.03.044>.

416 (31) Abraham, J.; Dowling, K.; Florentine, S. Effects of Prescribed Fire and Post-Fire Rainfall on  
 417 Mercury Mobilization and Subsequent Contamination Assessment in a Legacy Mine Site in  
 418 Victoria, Australia. *Chemosphere* **2018**, *190*, 144–153.  
 419 <https://doi.org/10.1016/j.chemosphere.2017.09.117>.

420 (32) Howard, D.; Macsween, K.; Edwards, G. C.; Desservetaz, M.; Guérette, E.-A.; Paton-Walsh, C.;  
 421 Surawski, N. C.; Sullivan, A. L.; Weston, C.; Volkova, L.; Powell, J.; Keywood, M. D.; Reisen,  
 422 F.; (Mick) Meyer, C. P. Investigation of Mercury Emissions from Burning of Australian  
 423 Eucalypt Forest Surface Fuels Using a Combustion Wind Tunnel and Field Observations.  
 424 *Atmospheric Environment* **2019**, *202*, 17–27. <https://doi.org/10.1016/j.atmosenv.2018.12.015>.

425 (33) Feinberg, A.; Dlamini, T.; Jiskra, M.; Shah, V.; Selin, N. E. Evaluating Atmospheric Mercury  
 426 (Hg) Uptake by Vegetation in a Chemistry-Transport Model. *Environ. Sci.: Processes Impacts*  
 427 **2022**, *24* (9), 1303–1318. <https://doi.org/10.1039/D2EM00032F>.

428 (34) Hurt, G. C.; Chini, L.; Sahajpal, R.; Frolking, S.; Bodirsky, B. L.; Calvin, K.; Doelman, J. C.;  
 429 Fisk, J.; Fujimori, S.; Klein Goldewijk, K.; Hasegawa, T.; Havlik, P.; Heinemann, A.;  
 430 Humpenöder, F.; Jungclaus, J.; Kaplan, J. O.; Kennedy, J.; Krisztin, T.; Lawrence, D.;  
 431 Lawrence, P.; Ma, L.; Mertz, O.; Pongratz, J.; Popp, A.; Poulter, B.; Riahi, K.; Shevliakova, E.;  
 432 Stehfest, E.; Thornton, P.; Tubiello, F. N.; van Vuuren, D. P.; Zhang, X. Harmonization of  
 433 Global Land Use Change and Management for the Period 850–2100 (LUH2) for CMIP6. *Geosci.  
 434 Model Dev.* **2020**, *13* (11), 5425–5464. <https://doi.org/10.5194/gmd-13-5425-2020>.

435 (35) Michelazzo, P. A. M.; Fostier, A. H.; Magarelli, G.; Santos, J. C.; de Carvalho, J. A. Mercury  
 436 Emissions from Forest Burning in Southern Amazon. *Geophys. Res. Lett.* **2010**, *37* (9), L09809.  
 437 <https://doi.org/10.1029/2009GL042220>.

438 (36) Melendez-Perez, J. J.; Fostier, A. H.; Carvalho, J. A.; Windmöller, C. C.; Santos, J. C.; Carpi, A.  
439 Soil and Biomass Mercury Emissions during a Prescribed Fire in the Amazonian Rain Forest.  
440 *Atmospheric Environment* **2014**, *96*, 415–422. <https://doi.org/10.1016/j.atmosenv.2014.06.032>.

441 (37) Soares-Filho, B. S.; Nepstad, D. C.; Curran, L. M.; Cerqueira, G. C.; Garcia, R. A.; Ramos, C. A.;  
442 Voll, E.; McDonald, A.; Lefebvre, P.; Schlesinger, P. Modelling Conservation in the Amazon  
443 Basin. *Nature* **2006**, *440* (7083), 520–523. <https://doi.org/10.1038/nature04389>.

444 (38) Roulet, M.; Lucotte, M.; Farella, N.; Serique, G.; Coelho, H.; Passos, S.; Mergler, D. Effects of  
445 Recent Human Colonization on the Presence of Mercury in Amazonian Ecosystems. *Water Air  
446 Soil Pollut.* **1999**, *112*, 297–313.

447 (39) Renard, K. G.; Foster, G. R.; Weesies, G. A.; McCool, D. K.; Yoder, D. C. Predicting Soil  
448 Erosion by Water: A Guide to Conservation Planning with the Revised Universal Soil Loss  
449 Equation (RUSLE). *Agriculture handbook* **1997**, *703*.

450 (40) Borrelli, P.; Robinson, D. A.; Panagos, P.; Lugato, E.; Yang, J. E.; Alewell, C.; Wuepper, D.;  
451 Montanarella, L.; Ballabio, C. Land Use and Climate Change Impacts on Global Soil Erosion by  
452 Water (2015–2070). *Proc. Natl. Acad. Sci. U.S.A.* **2020**, *117* (36), 21994–22001.  
453 <https://doi.org/10.1073/pnas.2001403117>.

454 (41) Borrelli, P.; Robinson, D. A.; Fleischer, L. R.; Lugato, E.; Ballabio, C.; Alewell, C.; Meusburger,  
455 K.; Modugno, S.; Schütt, B.; Ferro, V.; Bagarello, V.; Oost, K. V.; Montanarella, L.; Panagos, P.  
456 An Assessment of the Global Impact of 21st Century Land Use Change on Soil Erosion. *Nat  
457 Commun* **2017**, *8* (1), 2013. <https://doi.org/10.1038/s41467-017-02142-7>.

458 (42) Panagos, P.; Borrelli, P.; Meusburger, K.; Yu, B.; Klik, A.; Jae Lim, K.; Yang, J. E.; Ni, J.; Miao,  
459 C.; Chattopadhyay, N.; Sadeghi, S. H.; Hazbavi, Z.; Zabihi, M.; Larionov, G. A.; Krasnov, S. F.;  
460 Gorobets, A. V.; Levi, Y.; Erpul, G.; Birkel, C.; Hoyos, N.; Naipal, V.; Oliveira, P. T. S.;  
461 Bonilla, C. A.; Meddi, M.; Nel, W.; Al Dashti, H.; Boni, M.; Diodato, N.; Van Oost, K.;  
462 Nearing, M.; Ballabio, C. Global Rainfall Erosivity Assessment Based on High-Temporal  
463 Resolution Rainfall Records. *Sci Rep* **2017**, *7* (1), 4175. [04282-8](https://doi.org/10.1038/s41598-017-<br/>464 04282-8).

465 (43) Hengl, T.; De Jesus, J. M.; MacMillan, R. A.; Batjes, N. H.; Heuvelink, G. B. M.; Ribeiro, E.;  
466 Samuel-Rosa, A.; Kempen, B.; Leenaars, J. G. B.; Walsh, M. G.; Gonzalez, M. R. SoilGrids1km  
467 — Global Soil Information Based on Automated Mapping. *PLoS ONE* **2014**, *9* (8), e105992.  
468 <https://doi.org/10.1371/journal.pone.0105992>.

469 (44) Lugato, E.; Smith, P.; Borrelli, P.; Panagos, P.; Ballabio, C.; Orgiazzi, A.; Fernandez-Ugalde, O.;  
470 Montanarella, L.; Jones, A. Soil Erosion Is Unlikely to Drive a Future Carbon Sink in Europe.  
471 *Sci. Adv.* **2018**, *4* (11), eaau3523. <https://doi.org/10.1126/sciadv.aau3523>.

472 (45) Van Oost, K.; Quine, T. A.; Govers, G.; De Gryze, S.; Six, J.; Harden, J. W.; Ritchie, J. C.;  
473 McCarty, G. W.; Heckrath, G.; Kosmas, C.; Giraldez, J. V.; Da Silva, J. R. M.; Merckx, R. The  
474 Impact of Agricultural Soil Erosion on the Global Carbon Cycle. *Science* **2007**, *318* (5850), 626–  
475 629. <https://doi.org/10.1126/science.1145724>.

476